where $E_{syn(e)}$ (= 0 mV) is the reversal potential of non-NMDA excitatory amino-acid receptors. $g^{l}_{syn(int)}$ and $g^{m}_{syn(ext)}$ are the synaptic conductances for input from neurons $l \in L$ and $m \in M$, respectively. s^{l}_{int} and s^{m}_{ext} are synaptic gating variables for these synaptic inputs. To reduce computational costs, we assumed that synaptic conductances $g^{l}_{syn(int)}$ and $g^{m}_{syn(ext)}$ in Eq. (2) are uncorrelated to the corresponding synaptic gating variables s^{l}_{int} and s^{m}_{ext}, respectively. Consequently, we simplify Eq. (2) as:

$$I_{syn(e)} = \left(\bar{g}_{syn(int)} \cdot \bar{s}_{int} + \bar{g}_{syn(ext)} \cdot \bar{s}_{ext}\right)\left(V - E_{syn(e)}\right) \quad (3)$$

where $\bar{g}_{syn(int)}$ and $\bar{g}_{syn(ext)}$ are overall synaptic conductance for inputs from neurons $l \in L$ and $m \in M$, respectively. The values of $\bar{g}_{syn(int)}$ and $\bar{g}_{syn(ext)}$ were randomly assigned from a uniformly distributed probability density function ranging between 0 and 10 nS and between 0 and $\bar{g}_{syn(ext)\_max}$, respectively. The rationale for using uniformly distributed probability density function for synaptic conductance is discussed in Section 4.3. $\bar{s}_{int}$ and $\bar{s}_{ext}$ are mean synaptic gating variables for these synaptic inputs, which are expressed as:

$$\bar{s}_{int} = \overline{\sum_{l \in L} s^{l}_{int}}, \qquad \bar{s}_{ext} = \overline{\sum_{m \in M} s^{m}_{ext}} \quad (4)$$

Similarly, synaptic inputs from an inhibitory neuronal group N are expressed as:

$$I_{syn(i)} = \bar{g}_{syn(inh)} \cdot \bar{s}_{inh}\left(V - E_{Cl}\right) \quad (5)$$

where $\bar{g}_{syn(inh)}$ is the overall synaptic conductance for inputs from neurons $n \in N$, $\bar{s}_{inh}$ are the mean synaptic gating variable for inhibitory inputs, and E_{Cl} (= −90 mV) is the equilibrium potential of Cl^{-}. The values of $\bar{g}_{syn(inh)}$ were randomly assigned from a uniformly distributed probability density function ranging between 0 and $\bar{g}_{syn(inh)\_max}$.

Presynaptic action potentials activate synaptic gating variables. We applied the same, fast (decay time constant τ_s = 5 ms) kinetics to all synaptic gating variables (Butera et al. 1999b):

$$\frac{ds_i}{dt} = \frac{\left[(1 - s_i) \cdot s_\infty\left(V_i\right) - s_i\right]}{\tau_s} \quad (6)$$

$s_\infty(V_i)$ determines the steady-state postsynaptic receptor activation based on the membrane potential of presynaptic neuron i:

$$s_\infty\left(V_i\right) = \frac{1}{1 + \exp\left[\frac{(V_i - \theta)}{\sigma}\right]} \quad (7)$$

where $\theta = -10$ mV and $\sigma = -5$ mV.

In the present model, I_{NaP} produces a slowly depolarizing current and endows cells with a bursting property. The inherent burst frequency of a single bursting neuron is changed by the persistent Na^{+} current conductance, $\bar{g}_{NaP}$, with a fixed value of the reversal potential of passive leakage current E_L (−59 mV). Bursting activity does not occur for $\bar{g}_{NaP} \leq 2.45$ nS (Butera et al. 1999a). In order to simulate an inhomogeneous distribution of inherent burst frequency within a group, the values of $\bar{g}_{NaP}$ were randomly assigned from a uniformly distributed probability density function ranging between ($\bar{g}_{NaP\_max}$ − 0.5 nS) and $\bar{g}_{NaP\_max}$. Consequently, the inherent burst frequency of the neuronal group depends on $\bar{g}_{NaP\_max}$. The firing of Pre-I neurons always precedes the inspiratory burst recorded from the fourth cervical ventral root of the spinal cord (C4VR), although Pre-I burst sometimes does not accompany the inspiratory C4VR burst (Okada et al. 2007). In order to simulate this situation, the inherent burst frequency of *NeuronGroup1* must be greater than that of *NeuronGroup2*. Subsequently, in the present model, we set $\bar{g}_{NaP\_max}$ = 4.0 nS for *NeuronGroup1* and $\bar{g}_{NaP\_max}$ = 3.0 nS for *NeuronGroup2*. For these values of $\bar{g}_{NaP\_max}$ for *NeuronGroup1* and *NeuronGroup2*, their interburst period was, respectively, found to be 2.69 ± 0.13 s and 4.99 ± 0.42 s (computed from 9 simulation results).

We set $\bar{g}_{syn(ext)} = 0$ nS for *NeuronGroup1* and $\bar{g}_{syn(inh)} = 0$ nS for *NeuronGroup2*. $\bar{s}_{inh}$ of *NeuronGroup1* was calculated from membrane potentials of *NeuronGroup2* neurons and $\bar{s}_{ext}$ of *NeuronGroup2* was calculated from membrane potentials of *NeuronGroup1* neurons. To evaluate the effects of changes in strengths of excitatory and inhibitory synaptic connections on the coupling pattern between pFRG and preBötC bursting activities, we varied $\bar{g}_{syn(inh)\_max}$ of *NeuronGroup1* ranging between 0 and 6 nS and $\bar{g}_{syn(ext)\_max}$ of *NeuronGroup2* ranging between 0 and 2 nS.

2.3 Computational details

The differential equations were solved numerically using the fourth-order Runge-Kutta equation with a step size of 0.05 ms. However, the neuronal states were saved at an interval of 0.5 ms, which was sufficient to capture every action potential spikes of bursting neurons, to keep the stored files to manageable size. All algorithms were implemented in double precision routine in C♯.NET language and run on Pentium-based Windows XP computers. We waited for initial 60 s of simulation time for the behavior of the network to stabilize and then the simulated data were saved.

3 Results

As mentioned earlier, in the dual oscillator model, *NeuronGroup1* and *NeuronGroup2* represents pFRG and preBötC, respectively. However, during the presentation of results and discussion, we restrict the terms *NeuronGroup1* and *NeuronGroup2* to refer to the *modeled* pFRG and preBötC, respectively. Further, throughout the present model study, we define the period where preBötC/*NeuronGroup2* neurons burst synchronously as the inspiratory phase, and the rest of period where a majority of preBötC/*NeuronGroup2* neurons are quiescent as the expiratory phase.

3.1 Coupling pattern between pFRG and preBötC

We observed different patterns of coupling between *NeuronGroup1* and *NeuronGroup2* depending on strengths of excitatory and inhibitory synaptic connections ($\bar{g}_{\text{syn(ext)\_max}}$ and $\bar{g}_{\text{syn(inh)\_max}}$, respectively). Figure 2(a) depicts typical raster plots for various coupling modes observed. Horizontal segments in Fig. 2(a) represent bursting periods of all the 2×81 neurons constituting the *NeuronGroup1* and *NeuronGroup2*. For each burst of each neuron, the bursting period is defined as the period beginning from the instant when the membrane potential of the neuron rises above -20 mV while delivering the first spike of the burst to the instant when the membrane potential falls below -20 mV while delivering the final spike of the burst. Membrane potential trajectories of a typical neuron within *NeuronGroup1* and *NeuronGroup2* for the various coupling modes are depicted in Fig. 2(c); averaged population activities of *NeuronGroup1* and *NeuronGroup2* are depicted in Fig. 2(b).

The coupling modes were classified visually based on the averaged population activity. However, since the population activity and the individual neuron

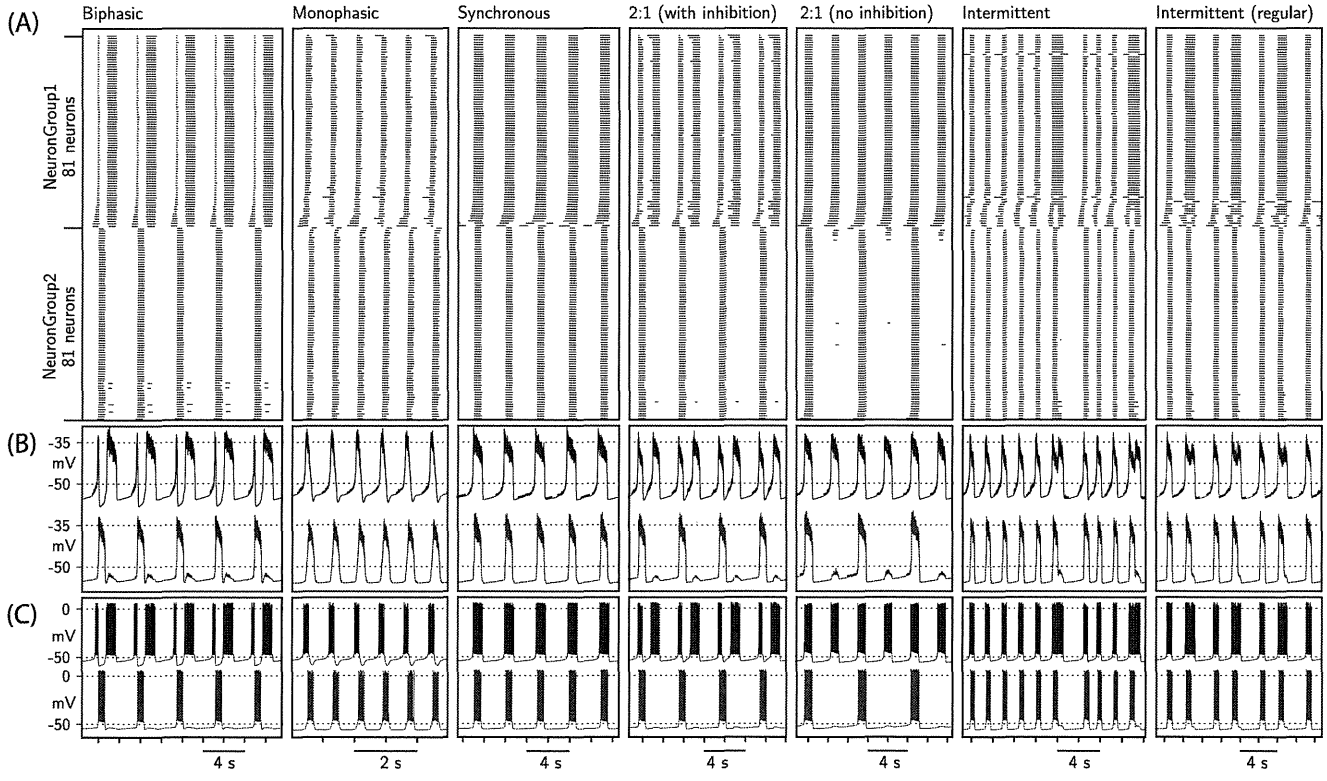

Fig. 2 (**a**) Raster plots of various coupling modes—biphasic ($\bar{g}_{\text{syn(ext)\_max}} = 0.8$ nS, $\bar{g}_{\text{syn(inh)\_max}} = 4.5$ nS), monophasic ($\bar{g}_{\text{syn(ext)\_max}} = 2.0$ nS, $\bar{g}_{\text{syn(inh)\_max}} = 5.0$ nS), Synchronous ($\bar{g}_{\text{syn(ext)\_max}} = 1.2$ nS, $\bar{g}_{\text{syn(inh)\_max}} = 0.5$ nS), 2:1 coupling (with inhibition: $\bar{g}_{\text{syn(ext)\_max}} = 0.8$ nS, $\bar{g}_{\text{syn(inh)\_max}} = 1.5$ nS; no inhibition: $\bar{g}_{\text{syn(ext)\_max}} = 0.4$ nS, $\bar{g}_{\text{syn(inh)\_max}} = 0.0$ nS), and intermittent ($\bar{g}_{\text{syn(ext)\_max}} = 2.0$ nS, $\bar{g}_{\text{syn(inh)\_max}} = 3.0$ nS; intermittent regular also corresponds to the same values of synaptic strengths)—observed by changing the strengths of excitatory and inhibitory synaptic conductances. The neurons within each neuronal groups are ranked in ascending order of their bursting activity initiation timings for better visualization. (**b**) Corresponding averaged population activity of *NeuronGroup1* and *NeuronGroup2* (*top* and *bottom traces*, respectively, in each panel) and (**c**) Activity of a typical neuron belonging to *NeuronGroup1* and *NeuronGroup2* (*top* and *bottom traces*, respectively, in each panel)

activity within the neuronal groups are well correlated, the coupling mode classification could be based on the activity of a pair of neurons from *NeuronGroup1* and *NeuronGroup2* as well (Fig. 2(c)). Nomenclatures used for classifying the different coupling pattern are as follows:

- The biphasic mode is characterized by activity pattern of *NeuronGroup1* neurons resembling Pre-I neurons—bursting just before inspiratory burst of *NeuronGroup2* neurons, inhibition during inspiratory phase, and post-inspiratory second burst (Fig. 2(c), Biphasic).
- The monophasic coupling mode is characterized by activity of *NeuronGroup1* neurons comprising two phases—bursting just before inspiratory burst of *NeuronGroup2* neurons and inhibition during inspiratory phase (Fig. 2(c), Monophasic). We termed this coupling mode as 'monophasic' because it may be thought of as a reduced form of biphasic coupling where the post-inspiratory second burst of *NeuronGroup1* neurons is missing. The bursting frequency of both *NeuronGroup1* and *NeuronGroup2* neurons are high in monophasic coupling mode; note the magnified time scale used for monophasic coupling in Fig. 2.
- The synchronous coupling mode is characterized by simultaneous bursting activity of both *NeuronGroup1* and *NeuronGroup2* neurons (Fig. 2(c), Synchronous).

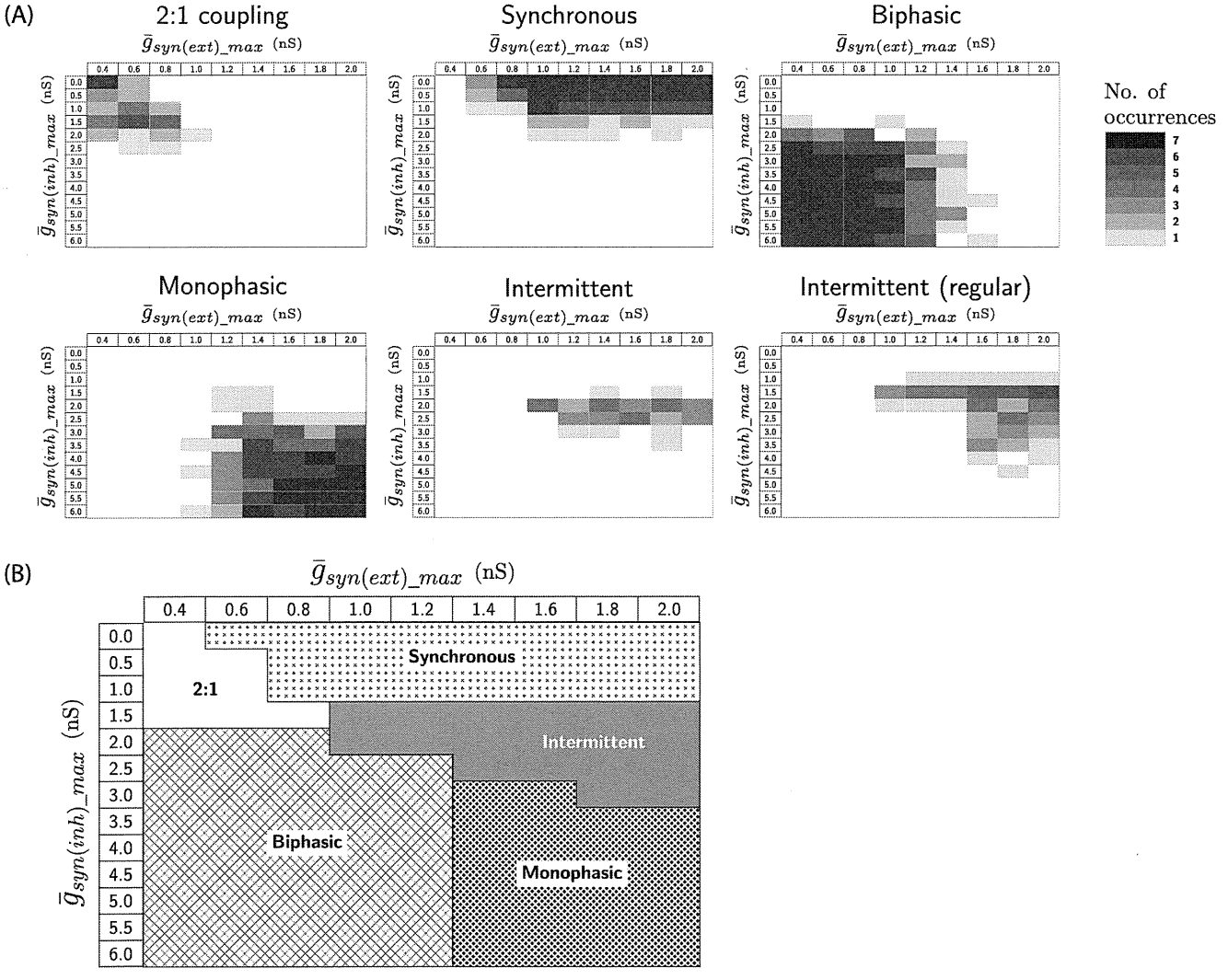

Fig. 3 (**a**) Domain of occurrence of coupling modes as a function of excitatory and inhibitory synaptic strengths of the dual oscillator model. For each combination of $\bar{g}_{\text{syn(ext)\_max}}$ and $\bar{g}_{\text{syn(inh)\_max}}$, seven simulations were performed and the frequency of occurrence of various coupling modes are illustrated using the gray color scale indicated on the *right*. (**b**) Representative domain of various coupling modes based on maximum occurrence frequency. For simplicity, the occurrence frequency of the two types of intermittent coupling modes were merged together, since their occurrence domain overlaps

- The 2:1 coupling mode is the case where *NeuronGroup1* and *NeuronGroup2* exhibit bursting activity in 2:1 ratio. 2:1 coupling mode may be further subclassified as (1) 2:1 with inhibition—*NeuronGroup1* neuron activity is similar to that of biphasic coupling mode except that its post inspiratory burst is significantly delayed (Fig. 2, 2:1 (with inhibition)), and (2) 2:1 without inhibition—*NeuronGroup2* neurons synchronize their bursting activity with every alternate bursting activity of *NeuronGroup1* neurons (Fig. 2, 2:1 (no inhibition)). In both of these 2:1 coupling modes, excitatory postsynaptic potentials (EPSPs) are observed on membrane trajectories of *NeuronGroup2* neurons coincident with the *NeuronGroup1* burst during the expiratory phase.
- Intermittent coupling mode shows mixed features of synchronous and monophasic coupling mode but with irregular variation in burst duration and interburst interval (Fig. 2, Intermittent). Frequently, we also obtained a more regular coupling between *NeuronGroup1* and *NeuronGroup2* for identical values of excitatory and inhibitory synaptic connections, which we termed as Intermittent (regular)—a pattern in which synchronous and monophasic coupling patterns are alternating (Fig. 2, Intermittent (regular)). Since the occurrence domain of Intermittent (regular) overlaps with that of the conventional Intermittent coupling (see Fig. 3, explanation for which is presented in the following paragraph), we decided to treat these two patterns collectively so as to gain some simplicity in the presentation of results.

Figure 3(a) shows the domain of various coupling modes observed as a function of $\bar{g}_{\text{syn(ext)\_max}}$ and $\bar{g}_{\text{syn(inh)\_max}}$. Seven simulations were done for each combination of $\bar{g}_{\text{syn(ext)\_max}}$ and $\bar{g}_{\text{syn(inh)\_max}}$ and the occurrence frequencies of each coupling mode are also shown. The boundaries of various coupling mode domains in Fig. 3(a) cannot be precisely determined, because the coupling modes changed slightly every time with the assignment of random initial values for the various synaptic conductance and $\bar{g}_{\text{NaP}}$ conductance. Figure 3(b) shows the domain of various coupling modes based on their maximum frequency of occurrence. It is remarked that occasionally the coupling patterns obtained in 2:1 coupling domain could not be meaningfully classified. The values of $\bar{g}_{\text{syn(ext)\_max}}$ and $\bar{g}_{\text{syn(inh)\_max}}$ are low in this region and thus the bursting behavior of *NeuronGroup1* and *NeuronGroup2* in some simulations were largely uncoupled.

3.2 Simulating the effects of decrease in preBötC neuronal excitability

We simulated the effect of decrease in preBötC neuronal excitability by increasing the leak current conductance $\bar{g}_{\text{L}}$ (used for the computation of leakage current

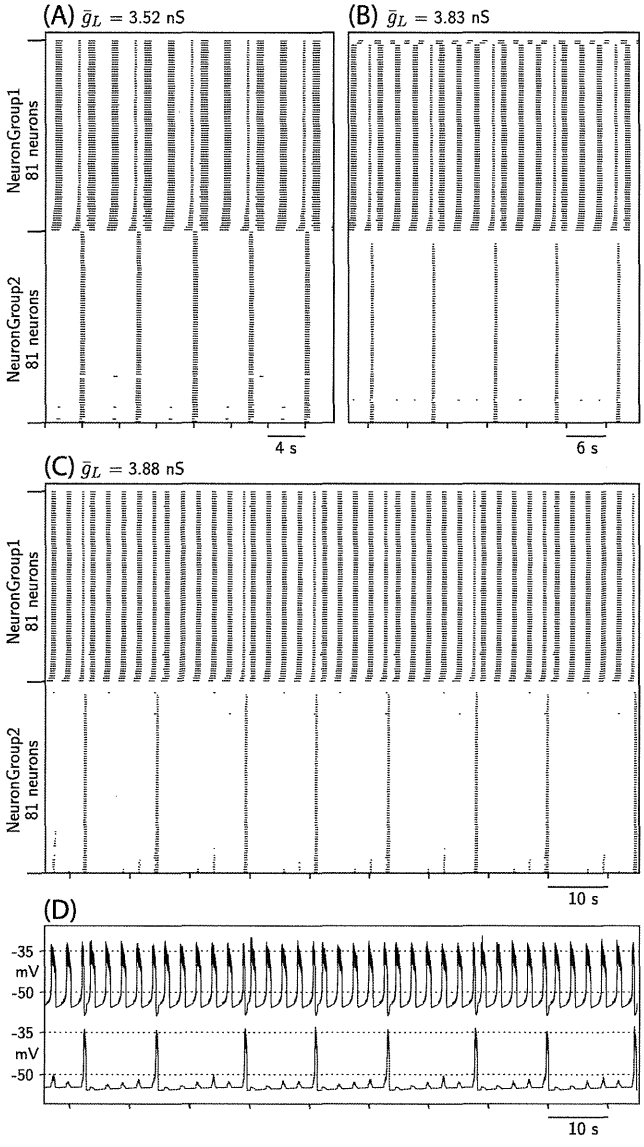

Fig. 4 Effect of increase in $\bar{g}_{\text{L}}$ value on the coupling mode between *NeuronGroup1* and *NeuronGroup2*. With the successive increase in $\bar{g}_{\text{L}}$, the coupling mode which is originally biphasic (Fig. 2(a), biphasic) changes to (**a**) 2:1 coupling, (**b**) 3:1 coupling and eventually (**c**) quantal slowing—*NeuronGroup2* exhibits bursting non-deterministically at fourth or fifth phasic excitations from *NeuronGroup1*. In raster plots, the neurons within each neuronal groups are ranked in ascending order of their bursting activity initiation timings for better visualization. (**d**) Averaged population activity of *NeuronGroup1* (*top trace*) and *NeuronGroup2* (*bottom trace*) corresponding to the quantal slowing case depicted in (**c**)

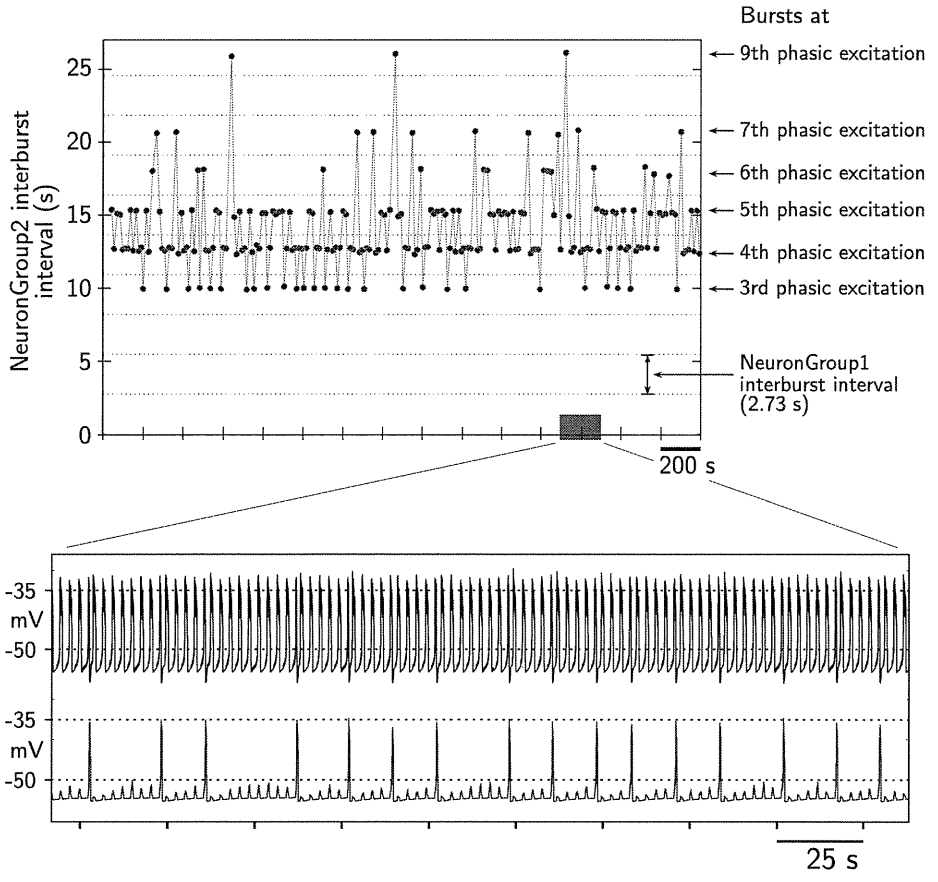

Fig. 5 (**a**) Plot depicting the non-deterministic variation of interburst interval of *NeuronGroup2* with time. The *vertical* separation between the *horizontal* grid lines indicates the interburst interval of *NeuronGroup1*. *NeuronGroup2* exhibits bursts, non-deterministically, at the third, fourth, fifth, sixth, seventh and ninth phasic excitatory drives from *NeuronGroup1*. (**b**) Population activities of *NeuronGroup1* and *NeuronGroup2* for the time interval depicted by the thick *gray bar* in (**a**). For the above simulation, the values of $\bar{g}_{\text{syn(ext)\_max}}$, $\bar{g}_{\text{syn(inh)\_max}}$ and $\bar{g}_{\text{L}}$ were 0.8 nS, 4.5 nS and 3.89 nS, respectively

I_{L} (Butera et al. 1999a)) for the neurons constituting *NeuronGroup2* and studied its effect on the coupling pattern using the dual oscillator model. We studied the case when $\bar{g}_{\text{syn(ext)\_max}} = 0.8$ nS and $\bar{g}_{\text{syn(inh)\_max}} = 4.5$ nS, which consistently produces a biphasic coupling pattern in our simulation (Figs. 3 and 2(a)). When $\bar{g}_{\text{L}}$ is increased, the number of cells with pacemaker property in *NeuronGroup2* decreases (Fig. 10). When $\bar{g}_{\text{L}}$ is increased beyond 3.4 nS, none of the *NeuronGroup2* neurons show pacemaker property. In this situation, *NeuronGroup1* is the sole rhythm generator, and *NeuronGroup2* is the inspiratory pattern generator triggered by *NeuronGroup1* due to the excitatory synaptic connection from *NeuronGroup1* to *NeuronGroup2* ($\bar{g}_{\text{syn(ext)\_max}} = 0.8$ nS). We observed 2:1 coupling, 3:1 coupling and eventually quantal slowing of bursting rhythms between *NeuronGroup1* and *NeuronGroup2* (Fig. 4), as the value of $\bar{g}_{\text{L}}$ was successively increased. In Fig. 4(c), *NeuronGroup2* non-deterministically exhibits bursts at the fourth or fifth phasic excitations from the *NeuronGroup1*. Figure 5 depicts the non-deterministic variability in the interburst interval of *NeuronGroup2* for a long duration simulation of quantal phenomenon; the quantal distribution of the interburst interval is readily apparent.

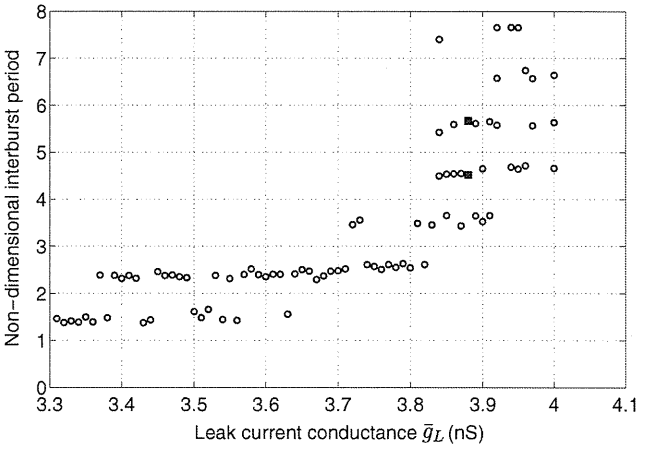

Fig. 6 Interburst interval of *NeuronGroup2* as a function of $\bar{g}_{\text{L}}$. The interburst interval of *NeuronGroup2* is non-dimesionlized to remove the variability in interburst interval of *NeurnGroup2* caused by variability in the interburst interval of *NeuronGroup1*. A new simulation is performed for each value of $\bar{g}_{\text{L}}$. For $\bar{g}_{\text{L}}$ <3.84 nS, we observed single bursting frequency of *NeuronGroup2*. Quantal slowing was observed in the range 3.84 nS $\leq \bar{g}_{\text{L}} \leq$ 4.0 nS; multiple data points corresponding to the same value of $\bar{g}_{\text{L}}$ in this range depicts the multiple interburst intervals observed. For example, the two *solid squares* depicts the the two interburst interval of *NeuronGroup2* obtained for the case $\bar{g}_{\text{L}} = 3.88$ nS shown in Fig. 4(c)

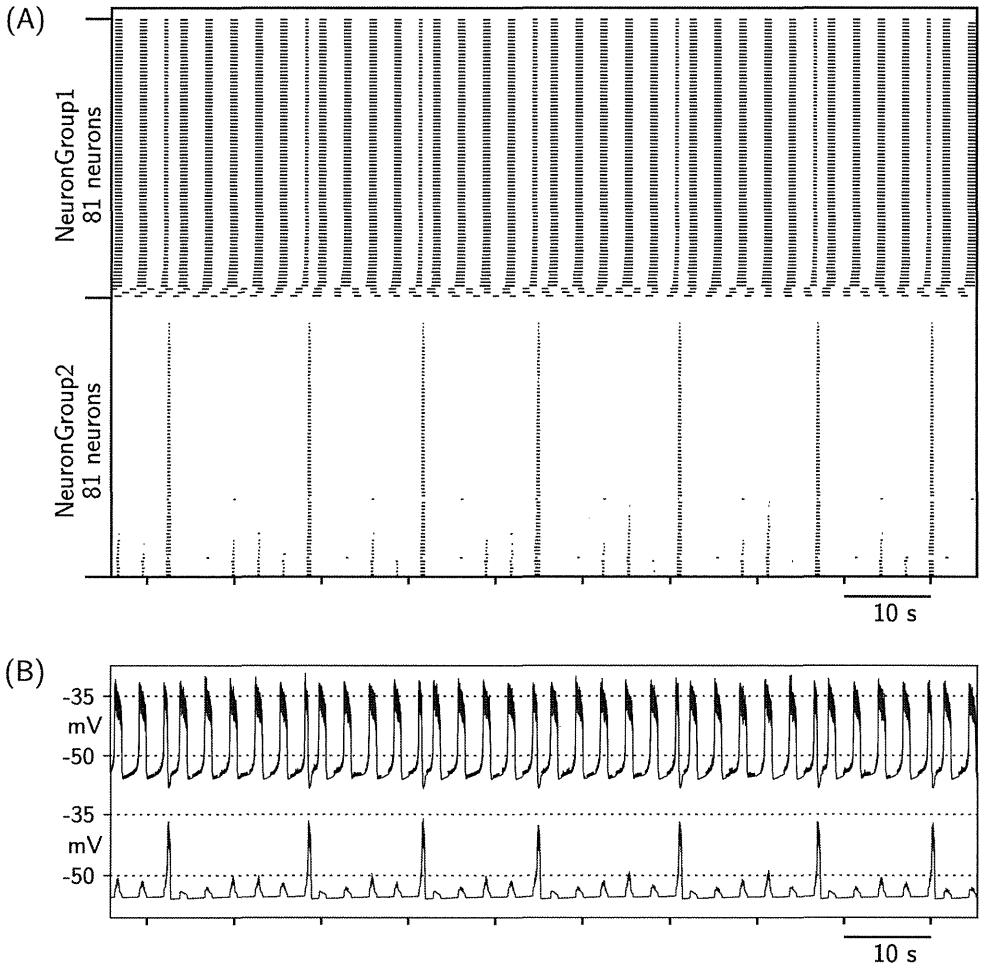

Fig. 7 Quantal slowing observed when $\bar{g}_{NaP\_max}$ of *NeuronGroup2* was reduced to 2.09 nS ($\bar{g}_{syn(ext)\_max}$ = 0.8 nS, $\bar{g}_{syn(inh)\_max}$ = 4.5 nS). (**a**) Raster plots depicting the bursting activity of neurons within *NeuronGroup1* and *NeuronGroup2*, and (**b**) Averaged population activity within *NeuronGroup1* and *NeuronGroup2* (*top* and *bottom trace*, respectively). In raster plot, the neurons within each neuronal groups are ranked in ascending order of their bursting activity initiation timings for better visualization

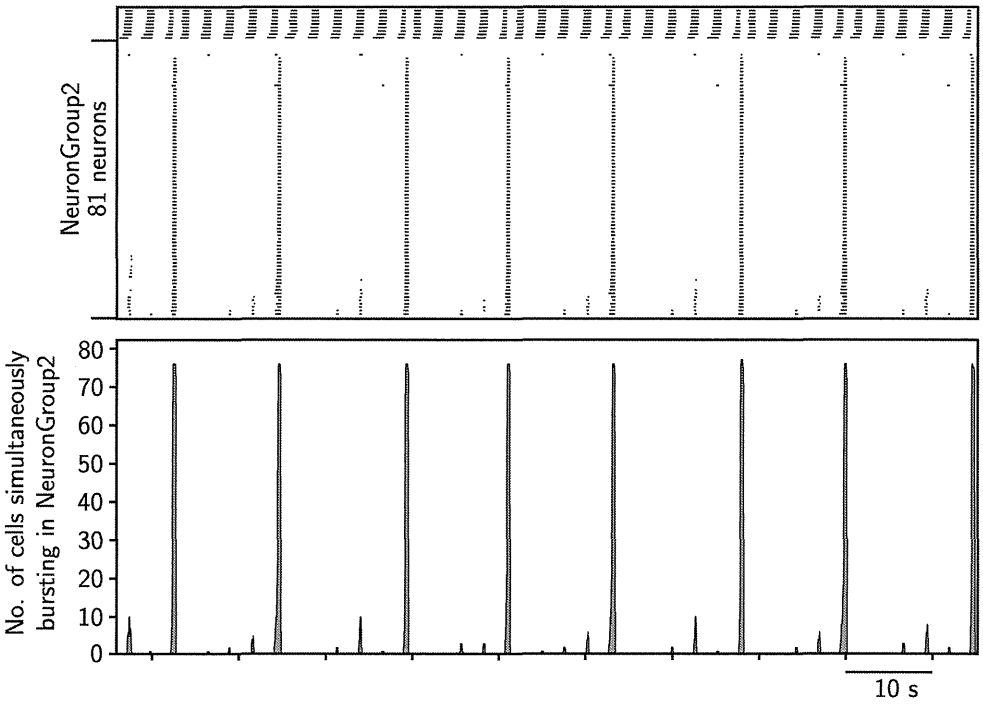

Fig. 8 Histograms showing the number of cells in *NeuronGroup2* exhibiting simultaneous bursting during the quantal slowing case depicted in Fig. 4(c)

However, the quantal slowing phenomenon was not observed in every simulation; the occurrence rate was about 70%; in the rest of the cases we obtained regular 4:1 or 5:1 coupling between *NeuronGroup1* and *NeuronGroup2*, similar to the regular 3:1 coupling depicted in Fig. 4(b). This was because, for every simulation, we assigned different random values to $\bar{g}_{NaP}$, $\bar{g}_{syn(int)}$, $\bar{g}_{syn(ext)}$, and $\bar{g}_{syn(inh)}$; the occurrence of quantal slowing was sensitive to the variability in bursting property of constituent neurons and distributions of the synaptic conductances.

Figure 6 depicts the interburst interval of *NeuronGroup2* as a function of $\bar{g}_L$. To make the quantal slowing effect apparent, the interburst interval of *NeuronGroup2* is non-dimensionalized with the interburst interval of *NeuronGroup1*. There is some variability in the interburst interval of the *NeuronGroup1* due to their random initialization. Since, at elevated values of $\bar{g}_L$ for neurons in *NeuronGroup2*, only *NeuronGroup1* is rhythm generator and *NeuronGroup2* bursts under the influence of excitatory phasic drives from *NeuronGroup1*, the variability in the interburst interval of *NeuronGroup1* is translated to variability in the interburst interval of *NeuronGroup2*. Non-dimensionlization eliminates this variability dependence and makes the quantal slowing effect pronounced.

The decrease in preBötC excitability is also simulated by reducing $\bar{g}_{NaP\_max}$ value of *NeuronGroup2*. When pursued this course, setting $\bar{g}_{syn(ext)\_max} = 0.8$ nS and $\bar{g}_{syn(inh)\_max} = 4.5$ nS in the dual oscillator model, we observed similar changes in coupling mode between *NeuronGroup1* and *NeuronGroup2* as depicted in Fig. 4 as the $\bar{g}_{NaP\_max}$ value was lowered; the coupling pattern successively changed from initial biphasic mode to 2:1 coupling, then to 3:1 coupling which eventually lead to quantal slowing. Figure 7 depicts a typical case of quantal slowing obtained by reducing $\bar{g}_{NaP\_max}$ value.

To gain insight into mechanism causing quantal slowing, further investigations were made. The histograms in Fig. 8 show the number of cells in the *NeuronGroup2* simultaneously bursting during the quantal slowing case depicted in Fig. 4(c). Almost all cells in *NeuronGroup1* showed synchronized activity and hence their activity is not shown. Note that a small fraction of neurons in the *NeuronGroup2*, variable in number, exhibited bursting by excitatory phasic drives from *NeuronGroup1* in the interval between successive synchronized *NeuronGroup2* bursting. Next, we removed the interconnections within *NeuronGroup2*, and investigated the number of neurons that exhibit bursting by phasic drives from *NeuronGroup1* under such condition. To do this, we set $\bar{g}_{syn(ext)\_max} = 0.8$ nS and $\bar{g}_{syn(inh)\_max} = 0$ nS, and for all *NeuronGroup2* cells, we set $\bar{g}_{syn(int)} = 0$.

Consequently, the dual oscillator model was modified as follows: (1) *NeuronGroup1* remains unchanged, (2) *NeuronGroup2* becomes essentially a group of unconnected 81 neurons, and (3) the excitatory synaptic connection from *NeuronGroup1* to *NeuronGroup2* is present ($\bar{g}_{syn(ext)\_max} = 0.8$ nS) but the inhibitory synaptic connection from *NeuronGroup2* to *NeuronGroup1* is absent. Subsequently, we successively increased the value of $\bar{g}_L$ for neurons in *NeuronGroup2* and studied the time history of neurons exhibiting bursting in *NeuronGroup2* quantitatively. Figure 9 depicts the details of one representative study when $\bar{g}_L = 3.85$ nS for neurons in *NeuronGourp2*. For the elevated value of $\bar{g}_L = 3.85$ nS, none of the neurons in *NeuronGroup2* possess pacemaker property (Fig. 10). However, under the influence of excitatory phasic drives from *NeuronGroup1*, a total of 19 (out of 81) neurons in *NeuronGroup2* exhibit bursting at various instances. Moreover, not all 19 neurons in *NeuronGroup2* exhibit simultaneous bursting;

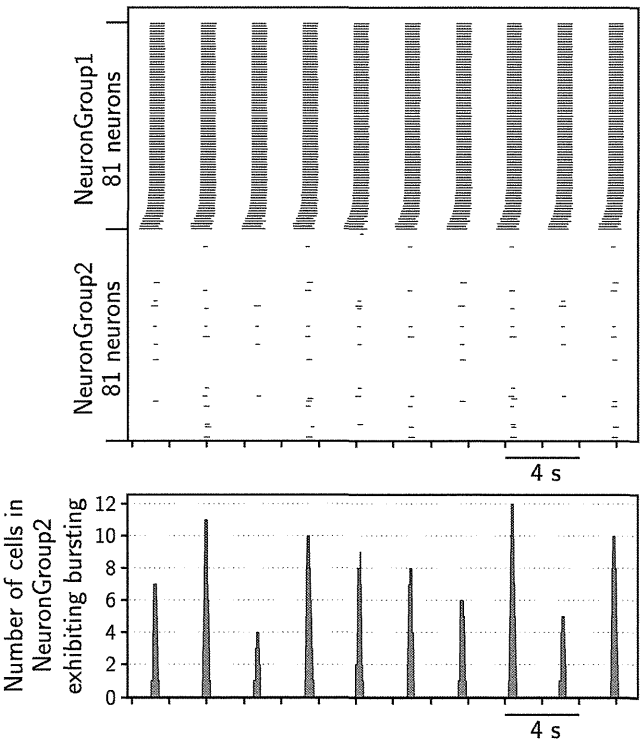

Fig. 9 Variability in the number of neurons in *NeuronGroup2* exhibiting bursting under the influence of excitatory phasic drive from *NeuronGroup1*. The neurons in *NeuronGroup2* are unconnected ($\bar{g}_{syn(int)} = 0$ nS for all neurons in *NeuronGroup2*) and $\bar{g}_{syn(ext)\_max} = 0.8$ nS and $\bar{g}_{syn(inh)\_max} = 0$ nS. In raster plot, the neurons within *NeuronGroup1* are ranked in ascending order of their bursting activity initiation timings for better visualization

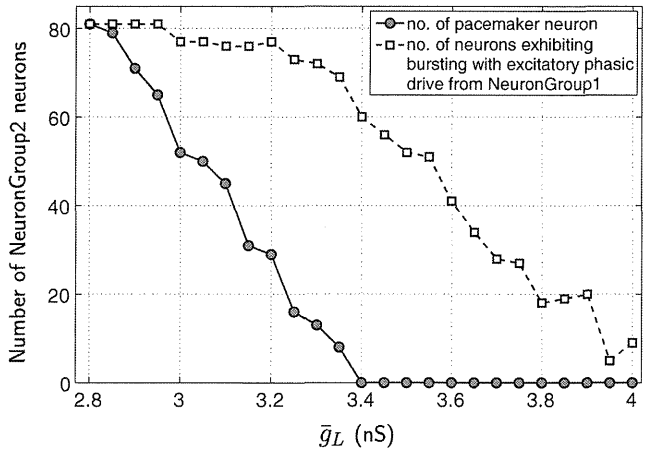

Fig. 10 Typical decrease in the number of neurons with pacemaker property in *NeuronGroup2* as $\bar{g}_L$ value is increased

the histograms in Fig. 9 show the variation in the number of neurons that exhibit simultaneous bursting at each excitatory phasic drive from *NeuronGroup1*. A maximum of 12 and a minimum of 4 neurons in *NeuronGroup2* exhibit simultaneous bursting, indicating that there is considerable variability. The number of neurons in *NeuronGroup2* that exhibit bursting with the influence of excitatory phasic drives from *NeuronGroup1* for different values of $\bar{g}_L$ is shown in Fig. 10.

4 Discussion

4.1 Coupling modes of pFRG and preBötC rhythm-generating networks

Our model could produce 1:1 coupling of bursting rhythms between pFRG and preBötC with the characteristic biphasic pre-inspiratory and post-inspiratory firing pattern of pFRG neurons. Post-inspiratory burst of *NeuronGroup1* neurons during biphasic coupling, characteristic of Pre-I neurons, is the consequence of recovery from I_{NaP} inactivation during inspiration-related inhibition of the Pre-I firing in our model (post-hyperpolarization rebound bursting (Butera et al. 1999a)).

Our results indicated that the coupling modes depend on the strengths of synaptic connections between the two networks. When we view the coupling modes as a function of the strengths of excitatory input from *NeuronGroup1* to *NeuronGroup2* ($\bar{g}_{syn(ext)\_max}$) and inhibitory input from *NeuronGroup2* to *NeuronGroup1* ($\bar{g}_{syn(inh)\_max}$), three major domains are recognized: (1) synchronous coupling domain with a low inhibitory strength, (2) biphasic coupling domain with a high inhibitory strength and low/moderate excitatory strength, and (3) monophasic coupling domain with high excitatory and high inhibitory strengths (Fig. 3). The changes in coupling mode by the inhibitory synaptic strength are consistent with experimental results. When a GABA antagonist (bicuculline or picrotoxin) or a glycine antagonist (strychnine) is given to the perfusate of brainstem spinal cord preparations, IIPI becomes absent or negligible, and the activity of Pre-I neurons overlaps with the C4VR inspiratory activity (Onimaru et al. 1990). These findings are in agreement with the model prediction when the strength of inhibitory connection from *NeuronGroup2* to *NeuronGroup1* is reduced.

Between the synchronous and biphasic major domains, there exists the domain of 2:1 coupling 'with inhibition' for moderate values of $\bar{g}_{syn(inh)\_max}$ (Fig. 3). The 2:1 coupling 'with inhibition' may be viewed as a precursor to biphasic coupling as the coupling mode transits from synchronous to biphasic with an increase in inhibitory strength. In the case of 2:1 coupling 'with inhibition', the inhibitory strength is not strong enough to cause an immediate post hyperpolarization rebound bursting of *NeuronGroup2* as in biphasic coupling; the bursting of *NeuronGroup2* is considerably delayed. We observed EPSPs in *NeuronGroup2* neuronal membrane trajectories coincident with the rebound bursts of *NeuronGroup1*. These EPSPs could not evoke *NeuronGroup2* burst because of two reasons: (1) low value of $\bar{g}_{syn(ext)\_max}$, and (2) the timing of excitatory inputs to *NeuronGroup2* from its previous burst is too close. With an increase in the value of $\bar{g}_{syn(ext)\_max}$, excitatory inputs to the neurons of *NeuronGroup2* increase, causing it to burst every time the pFRG bursts, thus transforming the 2:1 coupling to the intermittent coupling mode (Fig. 3).

Likewise, the 2:1 coupling 'without inhibition', which is primarily found to the left of the synchronous coupling domain and for extremely low values of inhibitory strength, may be viewed as a precursor to synchronous coupling. In 2:1 coupling 'without inhibition', the excitatory strength is not strong enough to cause a synchronized bursting of *NeuronGroup2* at each phasic excitation from *NeuronGroup1*; instead it synchronizes at every alternate phasic excitation from *NeuronGroup1*. It may be noted that the cases of 2:1 coupling 'with' and 'without inhibition' presented in Fig. 2 lie at the two extremities of the 2:1 coupling domain marked in Fig. 3(b); thus, the difference between them is readily evident. However, the transition from 'without inhibition' form of 2:1 coupling to 'with inhibition' form is extremely smooth; therefore, we merged the two cases

together while determining the coupling domains in Fig. 3.

As 2:1 'with inhibition' coupling mode transits to intermittent coupling mode with increase in the value of $\bar{g}_{syn(ext)\_max}$, biphasic mode transits to monophasic coupling mode with increase in the value of $\bar{g}_{syn(ext)\_max}$. For the biphasic coupling mode, the value of $\bar{g}_{syn(ext)\_max}$ is relatively low. Consequently, the EPSPs provided by *NeuronGroup1* at the time of its post inspiratory burst to *NeuronGroup2* is not sufficient to make it burst again. However, for higher values of $\bar{g}_{syn(ext)\_max}$, as in the case of monophasic coupling, the post-inspiratory burst of *NeuronGroup1* provides high enough EPSPs to *NeuronGroup2*, causing it to burst again (Fig. 2, Monophasic). Since the interval between pre-inspiratory and post-inspiratory bursts of *NeuronGroup1* is very small, the frequency of bursts in monophasic coupling mode is high. It may be observed that the excitation-inhibition cycle (excitation of *NeuronGroup2* by *NeuronGroup1* and inhibition of *NeuronGroup1* by *NeuronGroup2*) continues infinitely in monophasic coupling, whereas in case of intermittent coupling, the excitation-inhibition cycle intermittently breaks and restarts again. This suggests that the excitation-inhibition cycle is more stable when both $\bar{g}_{syn(ext)\_max}$ and $\bar{g}_{syn(inh)\_max}$ are high.

To illustrate the predictive capability of dual oscillator model, it was remarked earlier in this section that biphasic and synchronous coupling modes are experimentally observed cases. In the same regard, it may also be of significance to note that the 2:1 coupling 'with inhibition' as depicted in Fig. 2 and the 2:1 coupling depicted in Fig. 4(a) are also observed in experimental conditions (Okada et al. 2007), which adds to the predictive capability of the model.

4.2 Mechanisms of quantal slowing

During quantal slowing, subthreshold phasic drives to preBötC inspiratory neurons are observed coincident with the timing of skipped inspiratory burst. Based on this observation together with non-deterministic jumps of the bursting period to integer multiples of the control period, Mellen et al. (2003) have suggested that opioid-induced quantal slowing results from transmission failure from unaffected Pre-I neurons to depressed preBötC networks. In addition, they have also mentioned that noisy mutual coupling between the rhythmically active preBötC and the pFRG networks could be an alternative explanation of quantal slowing. Following this, Wittmeier et al. (2008) simulated the quantal slowing phenomenon by incorporating *stochastic* excitatory synaptic transmission from pFRG to preBötC and reducing its (mean) conductance by 12.5% of control. Thereby, they reinforced the suggestion that quantal slowing results from both transmission failure and noisy mutual coupling between pFRG and preBötC.

In the present study, however, quantal slowing was observed without assuming transmission failure or noisy interactions. Here we use the term 'transmission failure' specifically as a suppression of excitatory synaptic transmission from pFRG to preBötC. The results of the present study are both new and simple; 'simple' in the sense that the basic dual oscillator model by itself is adequate to simulate quantal slowing *without* incorporating any additional hypothesis like transmission failure or noisy mutual coupling. Nevertheless, under some experimental conditions, these processes may contribute secondarily to the *primary* mechanism of quantal slowing as explained in the following paragraph.

The quantal slowing phenomena stems from the fact that the synchronized bursting of *NeuronGroup2* is governed by the states of a small fraction of neurons in it that exhibit bursting by phasic excitatory drives from *NeuronGroup1* under elevated values of $\bar{g}_L$ or decreased values of $\bar{g}_{NaP\_max}$ for neurons in *NeuronGroup2* (Fig. 10). These small fraction of neurons provide excitatory inputs to the other quiescent neurons of *NeuronGroup2* and help them to burst. If the total number of neurons in *NeuronGroup2* exhibiting bursting exceeds a 'critical value', it results in a self-sustained chain of events where progressively larger number of neurons of *NeuronGroup2* exhibit bursting and eventually all the neurons in *NeuronGroup2* exhibit synchronized bursting. On the other hand if the number of bursting neurons in *NeuronGroup2* falls short of the critical value, then the neurons in *NeuronGroup2* do not exhibit synchronized bursting. Figure 9 depicted variability in the number of neurons in *NeuronGroup2* exhibiting bursting by excitatory phasic drives from *NeuronGroup1*. Though, the case presented in Fig. 9 corresponds to unconnected neurons in *NeuronGroup2*, it is likely that similar variability, albeit to a different degree, exists even when the neurons in *NeuronGroup2* are interconnected through chemical synapses. This is evident if one compares the similarity in the bursting activity of a small fraction of *NeuronGroup2* neurons in the interval between synchronized bursting in Fig. 8 (and Fig. 7) with that of the uncoupled neurons in *NeuronGroup2* depicted in Fig. 9. Consequently, the number of bursting neurons in *NeuronGroup2* exceeds the critical number intermittently and synchronized *NeuronGroup2* bursting occurs. This results in quantal slowing of synchronized

bursting of *NeuronGroup2*. From our simulation study, we observed that a maximum of about 15 neurons in *NeuronGroup2* exhibit bursting when *NeuronGroup2* fails to exhibit synchronized bursting. Thus, the 'critical number' of bursting neurons that necessarily be surpassed for synchronized *NeuronGroup2* bursting may be greater than 15 (out of 81) neurons. The critical number is expected to be fuzzy rather than precisely defined. The fuzziness stems from the fact that the distribution of $\bar{g}_{\mathrm{NaP}}$ and $\bar{g}_{\mathrm{syn(int)}}$ among *NeuronGroup2* neurons is randomly assigned. Moreover, the critical number is a function of the network topology as well (see Section 4.3). For a neuronal group where the constituent neurons are interconnected in a different way than what we have considered here, the critical number is different. However, the qualitative aspects of the results, such as intermittent failure of *NeuronGroup2* to exhibit synchronized bursting, are generally expected and could be an underlying mechanism of quantal slowing.

Quantal slowing was not observed in 30% of the simulations. In these cases, the distributions of random values of $\bar{g}_{\mathrm{NaP}}$ and $\bar{g}_{\mathrm{syn(int)}}$ within *NeuronGroup2* are such that its constituent neurons are relatively better synchronized. This was evident from visual observation of the raster plots obtained for these cases, which resembled the regular coupling pattern in Fig. 4(b). Consequently, there is no intermittent failure of *NeuronGroup2* to exhibit synchronized bursting and hence no quantal slowing is observed. In such cases, the activity of the neuronal groups, both *NeuronGroup1* and *NeuronGroup2*, may be essentially captured by replacing each of them with a single pacemaker neuron. This probably explains why Wittmeier et al. (2008) could not simulate quantal slowing phenomenon with their simplified model unless they incorporated stochastic synaptic transmission. The simplified model lacks the complexity necessary to capture the essential source of (*apparent*) non-determinism resulting the quantal slowing phenomenon (as discussed in the previous paragraph), which is intrinsic in the neuronal population model that we have considered. It is important to realize that the non-determinism associated with the occurrence of quantal slowing simulation is an 'apparent' one—the dual oscillator model used to simulate quantal slowing *is* deterministic; it is the nonlinearity present in the bursting behavior of individual neurons within the neuronal groups that result in non-deterministic-like intermittent synchronized bursts of *NeuronGroup2*. Thus, our results also hint toward the fact that quantal slowing may not necessarily be derived from any stochastic processes but may actually be a deterministic phenomena.

Figures 5 and 6 suggests that the interburst durations of *NeuronGroup2* while exhibiting quantal slowing are not integer multiples of the control period but are instead fractional multiples. Interestingly, this was elucidated by Wittmeier et al. (2008) as well, though they achieved it by incorporating a stochastic synaptic transmission. Consequently, it may be inferred that the fractional nature of quantal slowing is primarily a characteristic of dual oscillator models and is independent of the mechanism inducing the non-determinism.

4.3 Relation of preBötC neuronal network topology to quantal slowing

We have assumed that each neuron of *NeuronGroup2* is synaptically connected to every other neuron within *NeuronGroup2* ("all-to-all" connectivity). Consequently, the intra-neuronal group synaptic current $I_{\mathrm{syn(int)}}$ for individual neurons of *NeuronGroup2* (the first term on the right hand side of Eq. (2)) is:

$$I_{\mathrm{syn(int)}} = \left(\sum_{l\in L} g^{l}_{\mathrm{syn(int)}} \cdot s^{l}_{\mathrm{int}}\right)\left(V - E_{\mathrm{syn(e)}}\right) \tag{8}$$

where L is *NeuronGroup2*. However, we subsequently reduced the above equation to

$$I_{\mathrm{syn(int)}} = \bar{g}_{\mathrm{syn(int)}} \cdot \bar{s}_{\mathrm{int}}\left(V - E_{\mathrm{syn(e)}}\right) \tag{9}$$

(refer Section 2.2, in particular the reduction of Eq. (2) to Eq. (3)) and then randomly assigned values to $\bar{g}_{\mathrm{syn(int)}}$ from a uniformly distributed probability density function ranging between 0 and 10 nS. Since, $\bar{s}_{\mathrm{int}}$ is the same for all the neurons, it is primarily the variability in the values of $\bar{g}_{\mathrm{syn(int)}}$ across the neurons in *NeuronGroup2*, which contributes to the variability in the intra-neuronal synaptic currents for individual neurons of *NeuronGroup2*. From synchronization perspective, a neuron with low value of $\bar{g}_{\mathrm{syn(int)}}$ may be considered as weakly connected to rest of the neurons within *NeuronGroup2* and vice versa.

It is remarked that the reduction of Eq. (8) to Eq. (9) modifies the intrinsic homogeneity present in "all-to-all" network connectivity. If we randomly assign values to $g^{l}_{\mathrm{syn(int)}}$ from a uniformly distributed probability density function of any appropriate range, and perform the summation shown in Eq. (8), the variability in the individual values of $g^{l}_{\mathrm{syn(int)}}$ will be equalized resulting in almost homogeneous distribution of $I_{\mathrm{syn(int)}}$ across the neurons of *NeuronGroup2*. Homogenous distribution of $I_{\mathrm{syn(int)}}$ within *NeuronGroup2* would imply that each neuron is connected equally strongly to rest of the neurons within *NeuronGroup2*. Since this is unlikely to be the case in the *real* preBötC, we presume that

our way of introducing variability in the distribution of $I_{syn(int)}$ across the neurons of *NeuronGroup2* is qualitatively more realistic. The significance of the usage of uniformly distributed probability density functions for randomly assigning the values to $\bar{g}_{syn(ext)}$ and $\bar{g}_{syn(inh)}$ in the model may be interpreted similarly.

Now, since in our simulations, quantal slowing is observed primarily due to intermittent failure of *NeuronGroup2* to exhibit synchronized burst, it is remarked that the ability of *NeuronGroup2* to exhibit synchronized bursts is intrinsically dependent on its network topology, in particular, the distribution of $I_{syn(int)}$ across the neurons of *NeuronGroup2*. In the quantal slowing simulation, Fig. 4(c) for example, we observe that *NeuronGroup2* mostly exhibits synchronized bursts at every fourth phasic excitation from *NeuronGroup1* but frequently it skips the fourth phasic excitation from *NeuronGroup1* and bursts at the fifth phasic excitation. Thus, once *NeuronGroup2* has exhibited a synchronized burst, there is an element of (apparent) non-determinism whether it will exhibit its next synchronized bust at the fourth phasic excitation from *Neurongroup1* or not. However, in experimentally observed quantal slowing, preBötC elucidates non-determinism in its busting at each phasic excitation of pFRG (Mellen et al. 2003). We reason that this discrepancy is probably due to the difference in the neuronal network topology of real preBötC as compared to the one we have incorporated in *NeuronGroup2*.

Thus, it is remarked that the highlight of the present simulation study of quantal slowing is only its essential qualitative feature—the (apparent) non-determinism associated with bursting of preBötC—and the potential mechanism causing it. The quantitative features of quantal slowing may only be simulated by incorporating a more realistic network topology for *NeuronGroup2*.

4.4 Some additional simulation studies

In the model presented above, we introduced variability in bursting frequencies of the constituent neurons of *NeuronGroup1* and *NeuronGroup2* by providing variability in the allocated value of persistent Na^+ current conductance $\bar{g}_{NaP}$ of neurons. The variability in bursting frequencies may also be introduced by providing variability in the leakage current conductance $\bar{g}_L$ of neurons keeping the $\bar{g}_{NaP}$ value fixed. We pursued this course too and verified that all the qualitative features presented above remains unchanged. For this study, we randomly assigned $\bar{g}_L$ to neurons of each neuronal group from a uniform probability distribution function ranging from 2.3 to 2.8 nS; we set $\bar{g}_{NaP} =$ 3.5 nS for all neurons of *NeuronGroup1* and $\bar{g}_{NaP} =$ 2.5 nS for that of *NeuronGroup2*, so that the bursting frequency of *NeuronGroup1* is higher than that of *NeuronGroup2*.

Further, we used a Gaussian distribution (with a standard deviation of 0.3 nS about the mean values of $\bar{g}_{NaP} = 3.5$ nS for *NeuronGroup1* and $\bar{g}_{NaP} = 2.45$ nS for *NeuronGroup2*) instead of the uniform distribution, for allocating the values of $\bar{g}_{NaP}$ to individual neurons. Again the qualitative features of results obtained were essentially the same as presented above. Thus, it is suggested that the results presented in the manuscript are independent of the mode of introducing the variability in bursting frequencies of the constituent neurons of the neuronal groups.

5 Model justification

We assumed that the intrinsic bursting frequency of pFRG is faster than that of preBötC. This is a prerequisite for the consistent firing of pFRG neurons before the burst of preBötC neurons. To our knowledge, this assumption has never been tested experimentally. The intrinsic bursting rhythm of pFRG neurons, separated from preBötC can be monitored from the facial nerve rootlet, however, the inherent bursting frequency of the pFRG is difficult to determine because the rhythm is suppressed by pons or other brain regions with the facial nerve attached (Onimaru et al. 2006). In the dual oscillator model, we simulated by reversing the bursting frequencies of *NeuronGroup1* and *NeuronGroup2*, that is by setting $\bar{g}_{NaP\_max} = 3.0$ nS for *NeuronGroup1* and $\bar{g}_{NaP\_max} = 4.0$ nS for *NeuronGroup2*. We did not obtain the characteristic biphasic coupling for any combination of excitatory and inhibitory synaptic strengths (the range of synaptic strengths considered for this study was the same as that in Fig. 3).

We assumed that the persistent Na^+ current is responsible for rhythmic bursts of pFRG and preBötC neurons. This assumption has been recently contradicted. Pace et al. (2007a) have demonstrated that I_{NaP} does not contribute to inspiratory drive potential generation in the vast majority of preBötC neurons. Another intrinsically bursting neuronal group has been identified in the preBötC, which is dependent on a calcium-activated nonspecific cationic current (I_{CAN}) (Peña et al. 2004). However, the relative contribution of pacemaker properties and synaptic inputs to rhythm generation is likely to be dynamic (Johnson 2007). For example, during hypoxia, the respiratory pattern generator is more dependent on pacemaker properties and produces gasping behavior (Paton et al. 2006). Further

recent data of Koizumi et al. (2008) from neonatal rats contradict the data of Pace et al. (2007b) from mice, and show that inspiratory rhythm generation can be I_{NaP}-dependent in the isolated preBötC network *in vitro*. Therefore, although we did not consider I_{CAN}, the breakdown of synchronized burst could still be the underlying mechanism of quantal slowing in certain conditions.

It has been shown that glutamatergic excitatory synaptic inputs are required to evoke the I_{CAN}-dependent inspiratory drive potentials (Pace et al. 2007b), suggesting that the rhythmic burst is generated by a "group pacemaker" mechanism (Feldman and Del Negro 2006) in which rhythm generation is an emergent property of the network. Recently, Rubin et al. (2009) proposed a mathematical model of the neurons exhibiting "group pacemaker" mechanism. However, this model lacks the post-hyperpolarization rebound bursting dynamics which is essential for producing the post-inspiratory burst of pFRG, and thus we cannot use this neuronal model to simulate and study quantal slowing.

We simulated the opioid-induced reduction of excitability in preBötC bursting neurons both by increasing $\bar{g}_L$ and by reducing $\bar{g}_{NaP\_max}$. However, we do not know how opioids depress preBötC neurons. Opioids activate a G-protein-coupled inwardly rectifying potassium conductance known as G_{irk}, resulting in the hyperpolarization of neurons throughout the central nervous system (Williams et al. 1982; Wimpey and Chavkin 1991). Therefore, the depressant effect of opioids on preBötC may be reasonably simulated by an increase in $\bar{g}_L$. On the other hand, it is unlikely that opioids directly affect $\bar{g}_{NaP\_max}$ because pFRG bursting neurons, which are I_{NaP}-dependent (Onimaru et al. 1997), are not affected by opioids (Takeda et al. 2001; Janczewski et al. 2002).

Since the two putative rhythm-generating networks are embedded hierarchically in the central respiratory pattern-generating network in more intact animals (Smith et al. 2007), dynamic interactions among neuronal groups must not be so simple. Opioid-induced quantal slowing has been observed in juvenile (Mellen et al. 2003) and adult (Vasilakos et al. 2005) rats *in vivo*. These observations can be interpreted as the manifestation of dynamic interactions between *fundamental-level networks*. However, it has been reported that eupnea of *in situ* intra-arterially perfused rats persists following the blockade of the two burst-generating currents, I_{NaP} and I_{CAN} (St.-John 2008). Therefore, whether the dual oscillator configuration is the fundamental-level network component of eupnea or that of gasping remains to be clarified.

In summary, we developed a dual oscillator model to understand the dynamic interactions between pFRG and preBötC neurons. Our model essentially assumes (1) both pFRG and preBötC networks are rhythm generators, (2) preBötC receives excitatory inputs from pFRG, and pFRG receives inhibitory inputs from preBötC, and (3) persistent Na^+ current conductance and synaptic current conductances are randomly distributed. Our model could produce the characteristic behaviors observed experimentally in neonatal brainstem spinal cord preparations. The coupling mode depended on the strengths of excitatory and inhibitory connections of the oscillator. In contrast to the earlier suggestions, quantal slowing was observed without transmission failure (suppressed excitatory synaptic conductance) or noisy mutual interactions between the neuronal networks of the oscillator. Our study suggests that quantal slowing may actually be a deterministic phenomena and the non-determinism associated with it may only be an 'apparent' one. We suggest that quantal slowing results from inhomogeneous properties of individual cells within the oscillator and subsequent breakdown of synchronized bursting within the preBötC oscillator.

Acknowledgements This work was supported by the ISM Cooperative Research Program (2006-ISM-CRP-2029, 2007-ISM-CRP-2034), the 2006-2007 ISM Research Projects Grant, and Grants-in-Aid for Scientific Research from the Ministry of Education, Science, and Culture of Japan (19200021 and 20500360).

Open Access This article is distributed under the terms of the Creative Commons Attribution Noncommercial License which permits any noncommercial use, distribution, and reproduction in any medium, provided the original author(s) and source are credited.

References

Ballanyi, K., Onimaru, H., & Homma, I. (1999). Respiratory network function in the isolated brainstem-spinal cord of newborn rats. *Progress in Neurobiology, 59*, 583–634.

Barnes, B. J., Tuong, C. M., & Mellen, N. M. (2007). Functional imaging reveals respiratory network activity during hypoxic and opioid challenge in the neonate rat tilted sagittal slab preparation. *Journal of Neurophysiology, 97*, 2283–2292.

Butera, R. J., Rinzel, J., & Smith, J. C. (1999a). Models of respiratory rhythm generation in the pre-Bötzinger complex. I. Burting pacemaker neurons. *Journal of Neurophysiology, 81*, 382–397.

Butera, R. J., Rinzel, J., & Smith, J. C. (1999b). Models of respiratory rhythm generation in the pre-Bötzinger complex. II. Populations of coupled pacemaker neurons. *Journal of Neurophysiology, 81*, 398–415.

Feldman, J. L., & Del Negro, C. A. (2006). Looking for inspiration: New perspectives on respiratory rhythm. *Nature Reviews Neuroscience, 7*, 232–242.

Feldman, J. L., & Janczewski, W. A. (2006). Point: Counterpoint: The parafacial respiratory group (pFRG)/ pre-Bötzinger complex (preBötC) is the primary site of respiratory rhythm generation in the mammal. Counterpoint: The preBötC is the primary site of respiratory rhythm generation in the mammal. *Journal of Applied Physiology, 100*, 2096–2097.

Gray, P. A., Reckling, J., Bocchiaro, C., & Feldman, J. (1999). Modulation of respiratory frequency by peptidergic input to rhythmogenic neurons in the preBötzinger complex. *Science, 286*, 1566–1568.

Janczewski, W. A., Onimaru, H., Homma, I., & Feldman, J. L. (2002). Opioid-resistant respiratory pathway from the preinspiratory neurones to abdominal muscles: *In vivo* and *in vitro* study in the newborn rat. *Journal of Physiology, 545*, 1017–1026.

Johnson, S. M. (2007). Glutamatergic synaptic inputs and I_{CAN}: The basis for an emergent property underlying respiratory rhythm generation? *Journal of Physiology, 582.1*, 5–6.

Joseph, I. M. P., & Butera, R. J. (2005). A simple model of dynamic interactions between respiratory centers. In *Conf. proc. IEEE Eng. Med. Biol. Soc.* (Vol. 6, pp. 5840–5842).

Koizumi, H., Wilson, C. G., Wong, S., Yamanishi, T., Koshiya, N., & Smith, J. C. (2008). Functional imaging, spatial reconstruction, and biophysical analysis of a respiratory motor circuit isolated *in vitro*. *Journal of Neuroscience, 28*(10), 2353–2365.

Kuwana, S., Tsunekawa, N., Yanagawa, Y., Okada, Y., Kuribayashi, J., & Obata, K. (2006). Electrophysiological and morphological characteristics of GABAergic respiratory neurons in the mouse pre-Bötzinger complex. *European Journal of Neuroscience, 23*(3), 667–674.

Mellen, N. M., Janczewski, W. A., Bocchiaro, C. M., & Feldman, J. L. (2003). Opioid-induced quantal slowing reveals dual networks for respiratory rhythm generation. *Neuron, 37*, 821–826.

Okada, Y., Masumiya, H., Tamura, Y., & Oku, Y. (2007). Respiratory and metabolic acidosis differentially affect the respiratory neuronal network in the ventral medulla of neonatal rats. *European Journal of Neuroscience, 26*, 2834–2843.

Oku, Y., Masumiya, H., & Okada, Y. (2007). Postnatal developmental changes in activation profiles of the respiratory neuronal network in the rat ventral medulla. *Journal of Physiology, 585*, 175–186.

Onimaru, H., Arata, A., & Homma, I. (1988). Primary respiratory rhythm generator in the medulla of brainstem-spinal cord preparation from newborn rat. *Brain Research, 445*, 314–324.

Onimaru, H., Arata, A., & Homma, I. (1990). Inhibitory synaptic inputs to the respiratory rhythm generator in the medulla isolated from newborn rats. *Pflügers Archiv, 417*, 425–432.

Onimaru, H., Arata, A., & Homma, I. (1997). Neuronal mechanisms of respiratory rhythm generation: An approach using *in vitro* preparation. *Japanese Journal of Physiology, 47*, 385–403.

Onimaru, H., & Homma, I. (2003). A novel functional neuron group for respiratory rhythm generation in the ventral medulla. *Journal of Neuroscience, 23*, 1478–1486.

Onimaru, H., & Homma, I. (2006). Point: Counterpoint: The parafacial respiratory group (pFRG)/pre-Bötzinger complex (preBötC) is the primary site of respiratory rhythm generation in the mammal. Point: The pFRG is the primary site of respiratory rhythm generation in the mammal. *Journal of Applied Physiology, 100*, 2094–2095.

Onimaru, H., Kumagawa, Y., & Homma, I. (2006) Respiration-related rhythmic activity in the rostral medulla of newborn rats. *Journal of Neurophysiology, 96*, 55–61.

Pace, R. W., Mackay, D. D., Feldman, J. L., & Del Negro, C. A. (2007a). Role of persistent sodium current in mouse pre-Bötzinger Complex neurons and respiratory rhythm generation. *Journal of Physiology, 580*, 485–496.

Pace, R. W., Mackay, D. D., Feldman, J. L., & Del Negro, C. A. (2007b). Inspiratory bursts in the preBötzinger complex depend on a calcium-activated non-specific cation current linked to glutamate receptors in neonatal mice. *Journal of Physiology, 582*, 113–125.

Paton, J. F., Abdala, A. P., Koizumi, H., Smith, J. C., & St.-John, W. M. (2006). Respiratory rhythm generation during gasping depends on persistent sodium current. *Nature Neuroscience, 9*, 311–313.

Peña, F., Parkis, M. A., Tryba, A. K., & Ramirez, J. M. (2004). Differential contribution of pacemaker properties to the generation of respiratory rhythms during normoxia and hypoxia. *Neuron, 43*, 105–117.

Rubin, J. E., Hayes, J. A., Mendenhall, J. L., & Del Negro, C. A. (2009). Calcium-activated nonspecific cation current and synaptic depression promote network-dependent burst oscillations. *Proceedings of the National Academy of Sciences of the United States of America, 106*(8), 2939–2944.

Smith, J. C., Abdala, A. P., Koizumi, H., Rybak, I. A., & Paton, J. F. (2007). Spatial and functional architecture of the mammalian brain stem respiratory network: A hierarchy of three oscillatory mechanisms. *Journal of Neurophysiology, 98*, 3370–3387.

Smith, J. C., Ellenberger, H. H., Ballanyi, K., Richter, D. W., & Feldman, J. L. (1991). Pre-Bötzinger complex: A brainstem region that may generate respiratory rhythm in mammals. *Science, 254*, 726–729.

Smith, J. C., Ellenberger, H. H., Ballanyi, K., & Richter, D. W. (1992). Whole-cell patch-clamp recordings for respiratory neurons in neonatal rat brainstem *in vitro*. *Neuroscience Letter, 134*, 153–156.

St.-John, W. M. (2008). Eupnea of *in situ* rats persists following blockers of *in vitro* pacemaker burster activities. *Respiratory Physiology & Neurobiology, 160*, 353–356.

Takeda, S., Eriksson, L. I., Yamamoto, Y., Joensen, H., Onimaru, H., & Lindahl, S. G. (2001). Opioid action on respiratory neuron activity of the isolated respiratory network in newborn rats. *Anesthesiology, 95*, 740–749.

Vasilakos, K., Wilson, R. J., Kimura, N., & Remmers, J. E. (2005). Ancient gill and lung oscillators may generate the respiratory rhythm of frogs and rats. *Journal of Neurobiology, 62*, 369–385.

Williams, J. T., Egan, T. M., & North, R. A. (1982). Enkephalin opens potassium channels on mammalian central neurones. *Nature, 299*, 74–77.

Wimpey, T. L., & Chavkin, C. (1991). Opioids activate both an inward rectifier and a novel voltage-gated potassium conductance in the hippocampal formation. *Neuron, 6*, 281–289.

Wittmeier, S., Song, G., Duffin, J., & Poon, C. S. (2008). Pacemakers handshake synchronization mechanism of mammalian respiratory rhythmogenesis. *Proceedings of the National Academy of Sciences of the United States of America, 105*(46), 18000–18005.

Detection and Visualization Method of Dynamic State Transition for Biological Spatio-Temporal Imaging Data

Fumikazu Miwakeichi*, Yoshitaka Oku, Yasumasa Okada, Shigeharu Kawai, Yoshiyasu Tamura, and Makio Ishiguro

Abstract—**In the statistical analysis of functional brain imaging data, regression analysis and cross correlation analysis between time series data on each grid point have been widely used. The results can be graphically represented as an activation map on an anatomical image, but only activation signal, whose temporal pattern resembles the predefined reference function, can be detected. In the present study, we propose a fusion method comprising innovation approach in time series analysis and statistical test. Autoregressive (AR) models were fitted to time series data of each pixel for the range sufficiently before or after the state transition. Then, the remaining time series data were filtered using these AR parameters to obtain its innovation (filter output). The proposed method could extract brain neural activation as a phase transition of dynamics in the system without employing external information such as the reference function. The activation could be detected as temporal transitions of statistical test values. We evaluated this method by applying to optical imaging data obtained from the mammalian brain and the cardiac sino-atrial node (SAN), and demonstrated that our method can precisely detect spatio-temporal activation profiles in the brain or SAN.**

Index Terms—**Biomedical optical imaging, brain mapping, innovation approach, time series analysis.**

I. Introduction

RECENT progress in techniques to record biological signals offers detailed spatio-temporal information in the brain through various methods, e.g., functional magnetic resonance imaging (fMRI) and optical recording. The structure of fMRI data is four-dimensional, three of them are for space and one is for time axis. In other words, a time series corresponds to each spatial three-dimensional grid (voxel). The statistical significance of the brain activation can be evaluated by regression analysis or cross correlation analysis between the time series on each voxel and the reference function. This method is implemented in statistical parametric mapping (SPM) and has been widely used as a standard tool for analysis [1]. Then the distribution of test values such as t-values corresponding to regression coefficient or correlation coefficient is expressed on a certain slice of an anatomical image.

An optical imaging technique using a voltage-sensitive dye enables us to measure membrane potential changes in excitable tissue. The technique converts membrane potentials of cells to intensities of fluorescence emitted from the cells. Then the changes in fluorescence on the surface of certain regions of a brain preparation can be recorded using a high-speed high-sensitivity camera [2]–[4]. The structure of optical imaging data is three-dimensional, two of them are for space and one is for time axis. Although the structure of optical imaging data is similar to that of fMRI data, there has been no widely used method for data analysis. Respecting to this situation, Oku *et al.* [2], [3] and Okada *et al.* [4] applied time-lagged correlation analysis to optical imaging data to elucidate the mechanism of respiratory rhythm and pattern generation in the rat and frog brainstem. In the studies of rat brainstem [2], [4], they used fouth cervical spinal cord ventral root (C4VR) output signals that are equivalent to phrenic inspiratory burst activity as the reference function, and found appearances of earlier and simultaneous activities relative to the output signals in the regions of respiratory rhythm generators.

The advantage of regression analysis or cross correlation analysis is that the significance of the coefficients can be statistically evaluated. Moreover, the test values can be mapped on an anatomical image and it gives spatial information. However, still there have been several problems in these analyses. The regression or correlation analysis evaluates only the morphological resemblance between a time series and a reference function. If there is some activation pattern that does not resemble the reference function, then it cannot be detected. More seriously, in the case that the reference function cannot be defined, the data can hardly be analyzed by these methods.

In the field of time series analysis, innovation approach has been efficiently applied to detect the changes in signal dynamics. The dynamical properties of stationary time series,

Manuscript received August 10, 2010; revised December 15, 2010; accepted December 24, 2010. Date of publication January 10, 2011; date of current version March 02, 2011. This work was supported in part by grant-in-aid for scientific research of The Japanse Ministry of Education, Culture, Sports, Science, and Technology (No 19200021) and in part by grant-in-aid for scientific research of The Japanese Ministry of Education, Culture, Sports, Science, and Technology (No 19200021). *Asterisk indicates corresponding author.*

*F. Miwakeichi is with the Department of Statistical Modeling, The Institute of Statistical Mathematics, Tachikawa, Tokyo 190-8562, Japan (e-mail: miwake1@ ism.ac.jp).

Y. Oku is with the Department of Physiology, Hyogo College of Medicine, Nishinomiya, Hyogo 663-8501, Japan (e-mail: yoku@hyo-med.ac.jp).

Y. Okada is with the Department of Physiology, Hyogo College of Medicine, Nishinomiya, Hyogo 663-8501, Japan (e-mail: yasumasaokada@1979.jukuin.keio.ac.jp).

S. Kawai is with the Department of Data Science, The Institute of Statistical Mathematics, Tachikawa, Tokyo 190-8562, Japan (e-mail: s-kawai@zpost.plala.or.jp).

Y. Tamura is with the Department of Data Science, The Institute of Statistical Mathematics and the Department of Statistical Science, School of Multidisciplinary Sciences, The Graduate University for Advanced Studies, Tachikawa, Tokyo 190-8562, Japan (e-mail: tamura@ism.ac.jp).

M. Ishiguro is with the Department of Statistical Modeling, The Institute of Statistical Mathematics and the Department of Statistical Science, School of Multidisciplinary Sciences, The Graduate University for Advanced Studies, Tachikawa, Tokyo 190-8562, Japan (e-mail: ishiguro@ ism.ac.jp).

Color versions of one or more of the figures in this paper are available online at http://ieeexplore.ieee.org.

Digital Object Identifier 10.1109/TMI.2011.2104419

0278-0062/$26.00 © 2011 IEEE

whose statistical properties, e.g., mean value and variance, do not depend on time, can be identified using mathematical models such as autoregressive (AR) model and autoregressive moving average (ARMA) model. Let us suppose that we prepare two time series; one is used as a test time series for model identification, and the other is for filtering with the identified model. If new time series is filtered through the identified model, unpredictable signals remain in residuals. The residuals are called innovations. If the amplitude of innovations of filter output becomes significantly higher than the innovation of test data, the state is detected as a phase transition of dynamics in the system. This approach has been applied in various fields, e.g., plant monitoring system [6]–[10].

In the present study, we applied the innovation approach to optical imaging data obtained from the mammalian brain and the cardiac sino-atrial node (SAN), and attempted to detect biological activation in innovations. In addition, we propose a new method of statistical evaluation for the data set that is recorded in repeated measurement and a method for visualizing spatio-temporal distribution of the statistical test values.

II. Methods

A. Innovation Approach

The autoregressive (AR) model for a time series $\eta(t)$, $t = 1, \ldots, S$, is defined as a linear combination of the past values with a prediction error $\varepsilon(t)$ and a constant β

$$\eta(t) - \beta = \sum_{i=1}^{p} \alpha(i)\eta(t-i) + \varepsilon(t) \tag{1}$$

where p denotes the model order and $\alpha(i)$ are AR coefficients. The linear dynamic properties of the system can be identified with a parameter vector $\boldsymbol{\vartheta} = \{\alpha(1), \ldots, \alpha(p), \beta, \sigma_\varepsilon^2\}$, here σ_ε^2 is a variance of $\varepsilon(t)$. The innovations result from the residual time series can be estimated as

$$\varepsilon(t) = \eta(t) - \hat{\eta}(t) = \eta(t) - \left(\sum_{i=1}^{p} \alpha(i)\eta(t-i) + \beta \right) \tag{2}$$

and the signals that cannot be predicted by the linear AR process remain in the innovations. In other words, innovations are filter outputs through a linear AR process.

Considering an exogenous input $\gamma(t)$, $t = 1, \ldots, S$, the AR model can be generalized to an AR model with exogenous inputs (ARX) denoted as

$$\eta(t) - \beta = \sum_{i=1}^{p} \alpha(i)\eta(t-i) + \sum_{j=1}^{q} \phi(j)\gamma(t-j) + \varepsilon(t). \tag{3}$$

Suppose the measurement points of the imaging data are on the two dimensional pixel that are labeled by an index $v = (l, m)$ and only the influences of nearest neighbor upon each pixel are considered as exogenous inputs, the ARX model will be specialized as

$$\eta^v(t) - \beta^v = \sum_{i=1}^{p} \alpha^v(i)\eta^v(t-i) + \sum_{u \in \mathrm{N}(v)} \sum_{j=1}^{q} \delta^u(j)\eta^u(t-j) + \varepsilon^v(t) \tag{4}$$

where $\mathrm{N}(\boldsymbol{v})$ is a set of indices of the neighbor pixels to the pixel at $v = (l, m)$. Suppose neighbor pixels are restricted to the pixels, which contact with the edge of the pixel at the point v, a set of indices of neighbor pixels will be

$$\mathrm{N}(v) = \{(l+1, m), (l, m-1), (l, m+1), (l-1, m)\}. \tag{5}$$

The ARX model with the restricted neighbor pixels will be referred as nearest neighbor autoregressive model (NNAR) in this paper. The innovations for the pixel at v

$$\begin{aligned} \varepsilon(t)^v &= \eta^v(t) - \hat{\eta}^v(t) \\ &= \eta^v(t) - \left(\sum_{i=1}^{p} \alpha^v(i)\eta^v(t-i) + \sum_{u \in \mathrm{N}(v)} \sum_{j=1}^{q} \delta^u(j)\eta^u(t-j) + \beta^v \right) \end{aligned} \tag{6}$$

contain the signals which cannot be predicted by a linear AR process even though the spatial influences from the neighbors are taken into consideration.

B. Statistical Evaluation of Innovations and Graphical Representation

In the case imaging data are repeatedly recorded, we obtain multiple time series $\eta^{\boldsymbol{w}}(t)$, $t = 1, \ldots, S$, for each pixel ($w = (l, m, n)$, l and m are the indices of a pixel, n is the index of the repetition, $1 \leq n \leq N$) (Fig. 5). Suppose the NNAR model is identified with a limited period $t_1 \leq t \leq t_2$, any arbitrary selected other period $t_1' \leq t \leq t_2'$ can be filtered through the identified NNAR model. Let the innovations corresponding to the period for the NNAR model identification and for filtering $\varepsilon^{1,\boldsymbol{w}}(t)$ and $\varepsilon^{2,\boldsymbol{w}}(t)$, respectively. The amplitude level of $\varepsilon^{2,\boldsymbol{w}}(t')$ will increase at the time point t' when the unpredictable signals arise. Then the statistical significance can be evaluated by comparing the mean value between the innovations at t', $N^{-1}\sum_{n=1}^{N} \varepsilon^{2,(l,m,n)}(t')$ and whole innovations within the period $t_1 \leq t \leq t_2$, $(N(t_2 - t_1))^{-1}\sum_{t=t_1}^{t_2}\sum_{n=1}^{N} \varepsilon^{1,(l,m,n)}(t)$ by some statistical test. In this study, we employed standard t-test for this purpose. By shifting time point t', time-dependent t-values can be computed. Then time-dependent activation t-map, which shows dynamic state transition, can be obtained by repeating this procedure for all pixels.

This method detects not only biological activation as dynamic state transition but also some artifact inevitably. Some procedure for artifact discrimination has to be considered. There are mainly two types of artifacts. One is stationary oscillatory noise such as those caused by electric power supply (hum noise) and mechanical vibration of measurement system. This sort of artifacts can be identified by AR-type model, and then $\varepsilon^{1,\boldsymbol{w}}(t)$ will be close to Gaussian white noise. Therefore the oscillatory noise will not appear in $\varepsilon^{2,\boldsymbol{w}}(t')$, because these artifacts consist of predictable signals. The other is caused by nonstationary sporadic noise, and it will appear in $\varepsilon^{2,\boldsymbol{w}}(t')$ because it cannot be predicted by the identified AR-type model. This sort of artifact can be partly removed from final results such as activation t-map by setting a threshold for spatial cluster size and/or duration.

C. Time-Lagged Cross Correlation Analysis

The time-lagged cross correlation analysis provides temporal information of the appearance of the signals in the imaging data whose wave forms resemble predefined reference function [2]. Suppose $\eta^{\boldsymbol{v}}(t)$ is a time series of imaging data for a pixel $v = (l, m)$ and $\varphi(t)$ is a predefined reference function, the lagged cross correlation can be denoted as

$$R^v(\tau) = \eta^v(t)\varphi(t-\tau)/\sqrt{\overline{(\eta^v)^2}}\sqrt{\overline{\varphi^2}} \tag{7}$$

where τ is a relative time lag. A lagged correlation coefficient can be straightforwardly converted to a t-value. Then time dependent correlation t-map can be obtained if this procedure is repeated for all pixels. In the case $\tau = 0$, it will be ordinary cross correlation analysis.

D. Simulation

We intended to illustrate the effectiveness of the proposed method in this section with simulated data. The simulated data consist of sinusoidal and triangle waves that represent physiological activations superposed on a background oscillation. The background oscillation is generated by AR process defined as (1). The model order p, AR coefficients, constant level β and sampling frequency Fs are set to $p = 2$, $\alpha(1) = 1.84$, $\alpha(2) = -0.98$, $\beta = 0$ and Fs $= 50$ [Hz], respectively, in order to generate 3 Hz background oscillation that can be observed in actual data sets. The sinusoidal wave is defined as a cosine curve $-0.5 \cdot \cos(2\pi f \cdot (t-\delta)/\mathrm{Fs}) + 0.5$ ($f = 0.5$ Hz, $\delta = 1.0$ s, 1.0 s $\leq t \leq$ 2.0 s), which imitates the C4VR respiratory activity [Fig. 4(c)], and was used as the reference function for the time-lagged cross correlation analysis. The triangle wave is for an example of the signal whose waveform does not resemble the reference function. The onset time of triangle wave was set on the origin of the time axis, and the offset time was set on 0.52 s, the onset and offset time of sinusoidal wave were set on 1.0 s and 3.0 s, respectively [Fig. 1(a) and (b)]. We prepared 30 simulated data with generating different background oscillation. Fig. 1(c) and (d) show one of the simulated data with different values of the variance of prediction error in (1) ($\sigma^2 = 0.0025$ and 0.0256, respectively).

The AR model was identified on the period between -5.0 s and -3.0 s (101 time frames). Subsequently, the period between -1.0–4.24 s (263 time frames) was filtered through the identified AR model. Fig. 3 shows the temporal transition of the amplitude of innovations for all repetitions. The area A is a set of the innovations within the period for model identification ($\varepsilon^{1,\boldsymbol{w}}(t)$) and the line B is a set of innovations of filter output ($\varepsilon^{2,\boldsymbol{w}}(t')$) at the time t'. We evaluated the statistical significance of the difference of mean amplitude of the innovations in the area A and on the line B using standard t-test, and repeated the same procedure for the simulated data instead of the innovations. Fig. 2(a) and (c) displays the temporal transition of t-values of simulated data and innovations, respectively. The horizontal line in each figure corresponds to the significance level ($p = 0.05$).

In case the variance of prediction error is sufficiently small ($\sigma^2 = 0.0025$), the t-values correspond to the triangle and sinusoidal waves exceed the significance level for both the simulated data and innovations. As the variance of the prediction error is raised to 0.0256, the t-values of simulated data, which even do not correspond to these waves exceeds significant level, that is, it causes false positive error (Fig. 3(a) right). On the contrary, the t-values of innovations only which correspond to these waves exceed significance level (Fig. 3(c) right). It can be said that the false positive rate is well controlled in the t-test with the innovations.

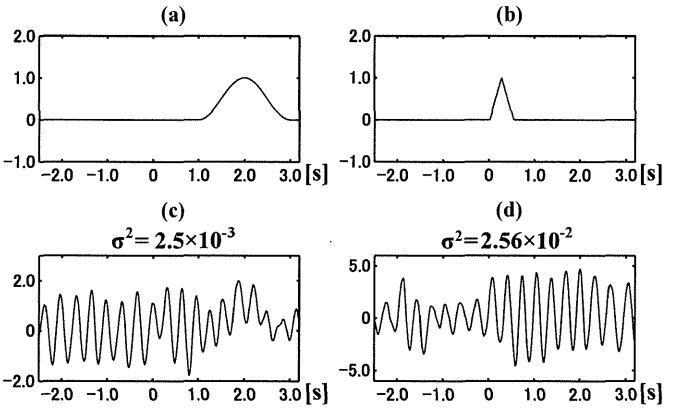

Fig. 1. The sinusoidal wave (a) and triangle wave (b) representing physiological activations. The simulated data with sinusoidal and triangle waves were superposed on the background oscillation generated by AR processes with different values of the variance of the prediction error (c), (d) ($\sigma^2 = 0.0025$ and 0.0256, respectively).

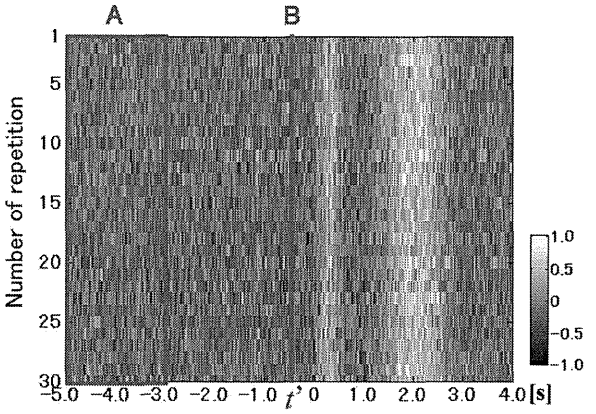

Fig. 2. Temporal transition of the amplitude of innovations for all simulated data (30 repetitions). The area A is the set of the innovations within the period of model identification and the line B is the set of the innovations of filter output at the time t'. The mean amplitude of innovations for each repetition was normalized between -1 to 1.

The results of the time-lagged correlation analysis between averaged simulated data and the predefined reference function [Fig. 1(a)] are shown in Fig. 3(b). Since a correlation coefficient can be computed with a relative time lag, the time axis indicates the relative time lag τ rather than the absolute time. And it is a natural consequence that the t-values have a maximal peak with $\tau = 0$. The t-values have also another peak at -1.74 s, which corresponds to the peak of the triangle wave. However it does not exceed the significance level, that is, it causes false negative error.

These algorithms were implemented in MATLAB 2006a and run on Windows XP computer (CPU: Intel Core2 Extreme Q6850 3 GHz, RAM: 3.25 GB). The computation time is about

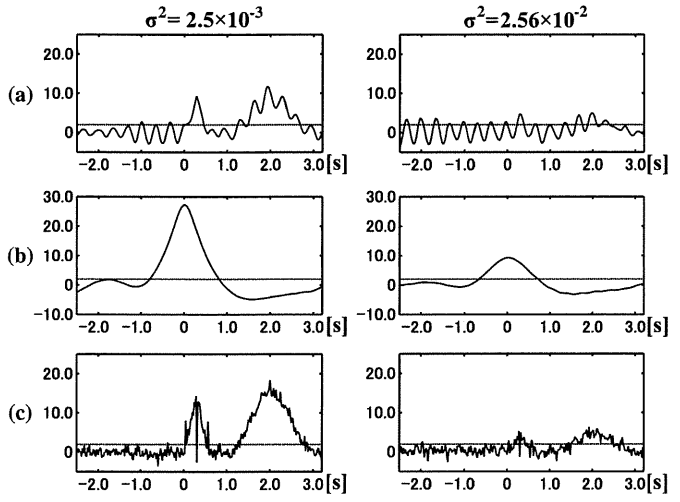

Fig. 3. Temporal transition of t-values for simulated data with different values of the variance of the prediction error (a), correlation coefficient with time lags (b), and innovations (c). The horizontal lime in each figure corresponds to the significance level of $p = 0.05$.

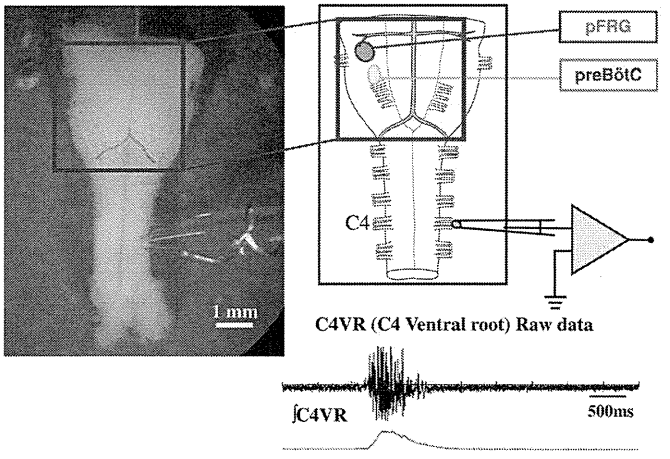

Fig. 4. (a) Ventral brainstem area for optical imaging (surrounded by the red square). (b) Schematic representation of anatomical structure of the brainstem and the recorded area. (c) Raw output signal from C4VR. (d) Integrated C4VR output signal.

30 minutes for innovation approach and about 10 minutes for cross correlation analysis with actual imaging data, except for the process for graphical representation.

III. Data Acquisition

We selected the same imaging data set from 2 day and 0 day old rats (corresponding to data1 and data2 respectively in this study) that was used in the study of developmental aspects of the respiratory neuronal activation in the rat brainstem [2] in order to evaluate our method by comparing its outputs with those of the time-lagged cross correlation analysis. Additionally, we analyzed the imaging data set from the rabbit cardiac sino-atrial node (SAN) as an example of the application of our method to other types of preparations (data3). These data were taken from the article that reported inhomogeneous action potential characteristics as a cause of pacemaker shift in the SAN [5].

The recording chamber was mounted on a fluorescence macro zoom microscope (MVX-10, Olympus Optical, Tokyo, Japan). Preparations stained with a voltage-sensitive dye were illuminated with a tungsten-halogen lamp (150 W) through a band-pass excitation filter ($\lambda = 480$–550 nm). Epifluorescence through a long-pass barrier filter ($\lambda > 590$ nm) was detected with a CMOS sensor array (MiCAM Ultima L-camera, BrainVision; 100 μm $\times$ 100 μm pixel size, 100 $\times$ 100 pixel array). Optical signals were sampled at 50 Hz (20 ms/frame) for data1 and data2, 500 Hz (2 ms/frame) for data3.

Analog signals of raw and integrated C4VR activities were recorded at 1 kHz for data1 and data2. The analog signal of electrical field potential of the SAN was recorded at 10 kHz for data3 with a pair of fine metal electrodes placed on both edges of the preparation. These analog signals were amplified and digitized, then stored in a hard disk together with optical signals. Analog signals were window-discriminated to yield transistor-transistor logic (TTL) pulses and used to trigger the optical recording system. Total number of recorded time frames were 1024/256/1024, the recording was started at 768/64/768 frames before the trigger signal, and repeated 30/34/71 times for data1/data2/data3, respectively. Among these repetitions, 29 and 27 repetitions, which were contaminated with relatively small artifacts, were selected for data1 and data2, respectively. In the case of data3, all repetitions had high enough quality, because SAN generated signals with high S/N ratio resulted from its highly synchronized activation. In order to set similar numbers of repetitions for all data sets, 30 repetitions were selected among 71 repetitions for a fair comparison with data1 and data2.

The change in fluorescence intensity (ΔF) relative to the initial intensity of the fluorescence (F_0) in each pixel was calculated. To normalize the difference in the amount of membrane-bound dye and illumination within the preparation, background fluorescence intensity at each pixel was divided by the maximum background fluorescence, and then the ratio of ΔF to the normalized background fluorescence intensity (F), i.e., the fractional change in fluorescence intensity ($\Delta F/F$), was calculated at each pixel in each frame. If F was less than 0.25, then $\Delta F/F$ was set to be zero [2]–[5]. Then the linear trend of imaging data associated with photobleaching was eliminated and z-transformed.

Fig. 4 shows the recorded area in the brainstem, which contains two putative rhythm generators reported as the para-facial respiratory group (pFRG) [12] and the pre-Bötzinger complex (preBötC) [13]. Inspiratory-related respiratory activity was monitored from the C4VR with a suction electrode. The raw nerve signal was amplified, band-pass filtered from 15 Hz to 3 kHz, full-wave rectified, and integrated with a decay time constant of 100 ms. This integrated signal was used as the reference function for the cross correlation analysis.

IV. Results

Background stationary oscillations were identified by a NNAR model on the period sufficiently before or after the respiration onset. In this study four neighboring pixels, which contact with edge of a pixel of interest were employed for the NNAR model for saving the computational cost. The parameters in the NNAR model were estimated using the least square method. Then the rest part of the data was filtered through the

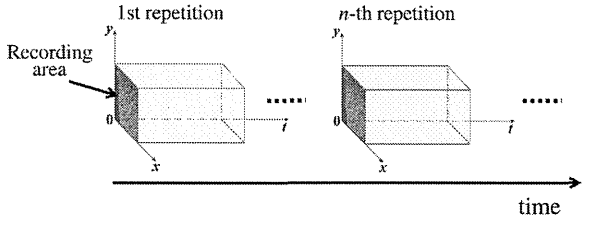

Fig. 5. Conceptual representation of the structure of the optical imaging data. The recorded imaging data can be reconstructed with three-dimensional data (two-dimensional space corresponding to recording area and time axis) for each repetition.

identified model and the innovations were estimated. We defined the origin of time axis as the onset of respiratory activity observed in the C4VR signal. The NNAR model was identified on the period sufficiently before the onset of respiratory activity, i.e., from -4.22 to -2.24 s (100 time frames). Subsequently, the period from -2.22 to 5.24 s (374 time frames) was filtered for the data1.

In order to investigate basic oscillatory properties of the data, we computed power spectrum using standard fast Fourier transformation (FFT). Fig. 6(c) shows averaged power spectrum across all pixels and all repetitions of imaging data and innovations. There were three major peaks in the power spectrum of the imaging data, which corresponded to about 0.1–0.5 Hz, 3.0–6.0 Hz, and 12.0–14.0 Hz, respectively. Spatial distribution map corresponding to these peaks are represented in Fig. 6(a). The spatial distribution pattern for 0.1–0.5 Hz nearly corresponded to the reported respiratory-related regions [2]. On the other hand, the latter two could correspond to stationary background oscillation originating from mechanical vibration of the recording system and/or turbulence associated with circulation of the perfusion fluid. Through this fundamental analysis, the respiratory activities appeared at a very low frequency of 0.1–0.5 Hz, whereas stationary background oscillations were seen at 3.0–6.0 Hz and 12.0–14.0 Hz ranges. In contrast, the peaks corresponding to the back ground oscillations significantly diminished in the power spectrum of innovations [Fig. 6(a)]. Moreover, spatial distribution maps were nearly homogenous, and any characteristic structure could not be observed, suggesting that the background stationary oscillations were accurately identified by the NNAR model and removed from the innovations. Because of the difference in the amplitude of imaging data and innovations, the intensity of power spectrum cannot be directly compared (the amplitude of innovations are smaller than imaging data). Therefore, the power spectrums were normalized.

In principle, model order of the NNAR model should be optimized according to some criterion, such as, Akaike information criterion (AIC) [14] for each pixel. However, since it would not be appropriate to individually optimize the model order for a large number of pixels, a common value should be chosen. It is important to choose a sufficiently large value, lest any relevant correlations in the data should be missed. On the other hand, too large model orders may cause over-fitting problems and reduce the reliability of the estimated model parameter values. In this study, the model order for p and q in (6) was fixed to the same values for the simplification of the model. We gradually

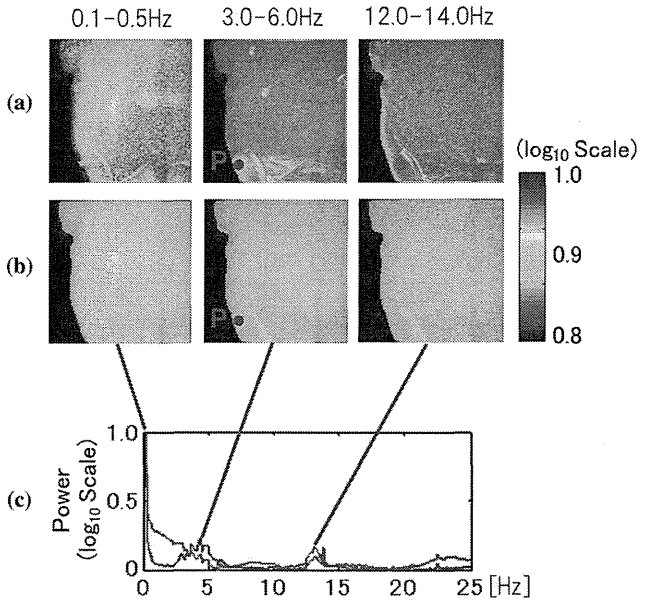

Fig. 6. Spatial distribution of averaged power spectrum in a limited frequency band for the optical recording data (a) and innovations (b). (c) Normalized averaged spectral power across all pixels and all repetitions for the optical recording data (blue line) and innovations (red line). The pixel on the point P is located in the region that was maximally contaminated with the background oscillation at 3.0–6.0 Hz. The raw imaging data and innovations correspond to this point and its eight neighbored pixels were used for further autocorrelation analysis.

increased the model order from two and found that stationary oscillations were properly identified and removed from the innovation by NNAR model with $p = q = 7$. Therefore we conclude that for our data a model order of this value represents a good compromise.

We further investigated whether the temporal correlation caused by background oscillation in the time series could be removed by NNAR model. The pixel at the point P in Fig. 6 is located in the region that was maximally contaminated with background oscillation at 3.0–6.0 Hz, and we selected this point as an example under severe condition. The autocorrelation functions of raw imaging data and innovations at the point P and its eight neighbored pixels were computed. Although autocorrelation functions of the imaging data contain strong temporal correlations at 4.0–5.0 Hz, the autocorrelation functions of innovations do not show any notable correlation (Fig. 7). These results indicate that the NNAR model could successfully reduce serial correlation from the imaging data.

We evaluated the statistical significance of the difference of mean amplitude of the innovations in the period of model identification and filter output by the method mentioned in Fig. 3. This procedure was repeated for all pixels, and then temporal transition of activation t-map was illustrated. Five representative time frames of activation time map are illustrated as time dependent t-maps in Fig. 8(c), which shows the area and time at which significant dynamic state transition arises. The activation initiated at the caudal part of pFRG, corresponding to the rostral ventrolateral medulla (RVLM) [12] and [15], and then extended rostrally toward the rostral part of pFRG and caudally toward the preBötC. Subsequently the activation traveled to more caudal structures of the brain. Finally the activation of the high cervical spinal cord reached its maximum (Fig. 8(c) in

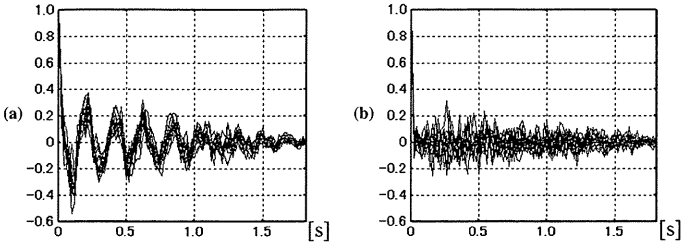

Fig. 7. Multiple plots of autocorrelation functions for raw imaging data (a) and innovations (b) corresponding to the pixel P in Fig. 6 and eight neighboring pixels. The signals of raw imaging data and innovations were z-transformed. The raw imaging data are contaminated with strong background oscillation at 4.0–5.0 Hz. On the contrary, any notable temporal correlation does not remain in the innovations, which are filter output of NNAR model.

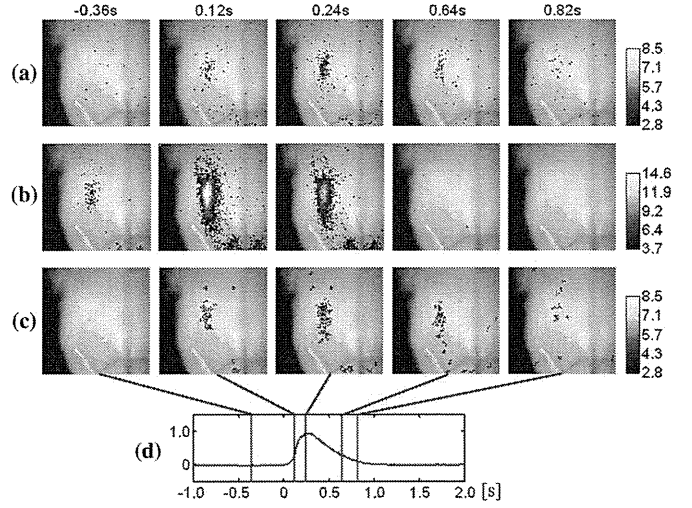

Fig. 8. Representative time frames of temporal transition of the activation t-maps for the imaging data (a) and the innovations (c), and the correlation t-map with averaged imaging data across repetition (b). The C4VR output signal and time points corresponding to the time frames (d). The t-maps were thresholded of $p < 0.05$ [corrected by the false discovery rate (FDR)] and a cluster extent of five pixels.

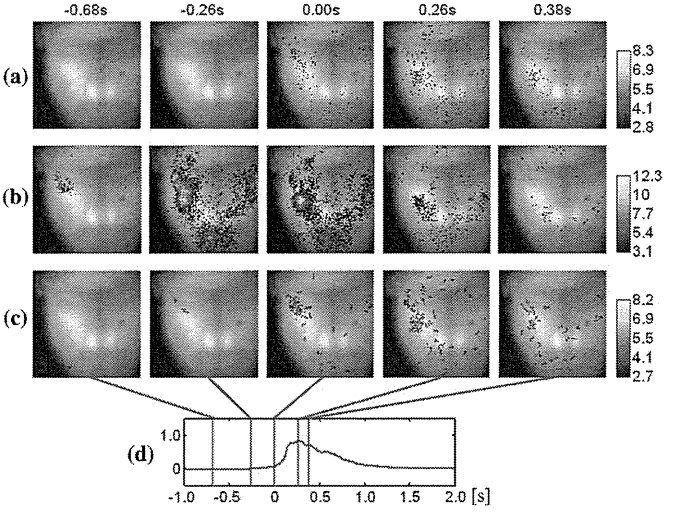

Fig. 9. Representative time frames of temporal transition of the activation t-maps for the imaging data (a) and the innovations (c), and the correlation t-map with averaged imaging data across repetition (b). The C4VR output signal and time points corresponding to the time frames (d). The t-maps were thresholded of $p < 0.05$ (corrected by the FDR) and a cluster extent of five pixels.

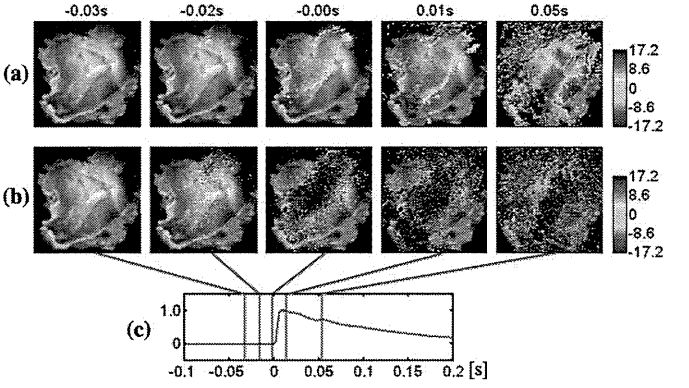

Fig. 10. Representative time frames of temporal transition of the activation t-maps for the imaging data from the rabbit cardiac sino-atrial node (SAN) (a) and the innovations (b). The C4VR output signal and time points corresponding to the time frames (d). The t-maps were thresholded of $p < 0.05$ (corrected by the FDR) and a cluster extent of five pixels.

the time frame at 0.24 s) just before the peak of C4VR output signals [Fig. 8(d)]. Further, a line from preBötC toward caudal brain structures could be seen in Fig. 8(c) in the time frame at 0.64 s. This sequence may correspond to the fact that caudal brain structures such as ventral respiratory group (VRG) contain premotor and motor neurons that relay respiratory outputs to the C3-5 segments of the spinal cord with a certain time delay.

Fig. 8(a) displays activation t-maps for the raw imaging data instead of the innovations using the procedure described above. Although both images for the imaging data and innovations were thresholded at the same level, significant areas for the imaging data were less than those for the innovations. Further, the propagation from the preBötC toward caudal brain structures could not be detected in activation t-maps for the raw imaging data.

The results of correlation analysis with averaged imaging data across repetitions are illustrated in Fig. 8(b) as correlation t-maps. The respiratory related activated areas, such as pFRG and preBötC, were effectively detected. However, the duration of detected activations was shorter than that of activation t-maps for the innovations. Besides, the propagation from the preBötC toward caudal brain structures could not be detected.

Data2 did not have enough time frames before the onset of respiratory activation because of the parameter setting for setting recording condition. Therefore the analysis cannot be applied to data2 under the same condition for data1. In order to solve this problem, the NNAR model was identified at the period sufficiently after the offset of respiration, i.e., from 1.98 to 3.96 s (100 time frames), and then the period from -1.12 to 1.96 s (155 time frames) was filtered. The activation t-maps for the imaging data and innovations are illustrated in Fig. 9(a) and (c), respectively. The correlation map is shown in Fig. 9(b). The analyses yielded similar results to those for data1. Furthermore, the time lag of the activation between preBötC and VRG could be clearly detected in the activation time map for the innovations (Fig. 9(c) in the time frames of 0 s and 0.26 s), which was not distinct in the correlation map [Fig. 9(b)].

We attempted to apply our method to other type of data, i.e., voltage imaging data of the SAN, in order to evaluate the performance of our method. The recorded electrical field potential of the SAN may be employed as the reference function for cross correlation analysis. However, the imaging data after the peak were contaminated with heavy artifact and the tissue was deviated from its original positions because of periodic contraction of the SAN. Therefore the cross correlation analysis was not appropriate for the imaging data of SAN.

On the contrary, our method was applicable, even though there was an artifact contamination in some temporal region. The NNAR model was estimated on the period sufficiently before the onset of action potential, from -0.23 s to -0.114 s (59 time frames), and then the period from -0.112 s–0.466 s (290 time frames) was filtered.

Fig. 10 shows activation t-maps for raw imaging data and innovations. Although the maps were thresholded with the same level, detected activation areas for the innovations were larger than those for the imaging data. Moreover, the beginning of the activation was sensitively detected for the innovations (in the time frame at -0.03 s). The propagation of action potential could be observed. The regions with negative t-values in the time frame at 0.05 s corresponded to the trough caused by the contraction artifact.

V. Discussion

Using the ordinary cross correlation analysis, which is equivalent to the time-lagged cross correlation analysis with a restriction $\tau = 0$, only one of the two respiratory rhythm generators, the preBötC, was detected with data2. The result can be seen in Fig. 9(b) in the time frame at 0.00 s. The reason why the other respiratory rhythm generator pFRG was missed is that the activation of pFRG appeared earlier than the onset of the C4VR activity in the reference function. Therefore significant correlation was not found between pFRG and C4VR signals. In this situation, time-lagged cross correlation analysis gave a solution. Oku, *et al.* [2] applied this method to the optical imaging data and reported an earlier respiratory activation in the pFRG [Fig. 9(b)].

However, there are still several problems remain in the ordinary or time-lagged cross correlation analysis. First, it does not consider dynamical properties of time series, but evaluates only morphological resemblance between two time series. Therefore only pixels whose temporal activity pattern has a similar shape to the reference function can be detected. Second, it has been applied only to averaged imaging data across the repetition of means. Any method has not been proposed that can be applied to each repetition nor statistically evaluated across the repetition of the measurement. Third, in the case of the time-lagged correlation analysis, the larger the time lag is, the shorter the overlapping length of the two time series becomes. Then, inaccuracy of the analysis will increase with larger time lags. Fourth, the absolute time point of the appearance of activations cannot be investigated by time-lagged cross correlation analysis. This is because the origin of time axis is defined arbitrarily. Therefore the correlation t-map of averaged imaging data and activation t-map for innovations cannot be compared on the common time axis. If the time point corresponding to the peak of C4VR signal is selected as the origin of time frame for the time-lagged cross correlation, the time point of the onset of activations in the correlation t-map and activation t-map will agree.

Our method is free from the above-mentioned problems. Namely, our method can sensitively detect the spatio-temporal emergence of activations through the investigation of the dynamic state transition and statistical evaluation across the repetition of the measurement. The earliest activation is localized in RVLM (the caudal part of pFRG), which can be seen typically with data2 (Fig. 9(c) in the time frame at -0.26 s). The activation extends bidirectionally to the rostral part of pFRG and to the preBötC region and travels to the high cervical spinal cord (Fig. 8(c) in the time frame at 0.64 s, and Fig. 9(c) in the time frame at 0.26 s). In the case of imaging data of SAN, the onset of activation could be detected by our method at least 0.01 s earlier than the result from the analysis using imaging data instead of innovations (Fig. 10(b) in the time frame at -0.03 s).

In this study, we analyzed the data that were recorded with multiple repetitions. Fig. 3 shows the temporal transition of the amplitude of innovations that was estimated in the simulated data. In the case of the data with single repetition, the line B will consist of only one innovation. Therefore, mean amplitudes of the innovations in the area A and on the line B cannot be statistically evaluated because of the insufficient number of samples. Nevertheless, our method is applicable if the line B is replaced with a time window in order to obtain sufficient number of samples, i.e., innovations, although there is a trade-off with respect to temporal resolution.

In order to estimate a neuronal network system, several methods, e.g., correlation analysis and Akaike causality [16], have been used. Whichever method is chosen, if it is directly applied to imaging data, a huge number of combinations of pixels have to be considered. This is not realistic, even though it could be done. Therefore, another procedure to extract a functional network structure from the imaging data is necessary. In order to avoid these problems, the regions of interest (ROIs) to estimate the network need to be set by preliminary analysis. In our method, the detected regions, where dynamic state transitions arose, may have spatial dynamic correlation associated with anatomical connections and play substantial roles to form a functional network structure. Namely, our method serves as a new approach to define ROIs and estimate functional network structures consistently.

We conclude that our method can precisely detect the biological activation without employing additional information such as reference time series data, and the significance can be evaluated with statistical test values. Further, it can be generally used to spatio-temporal data, e.g., fMRI, electroencephalography, near infrared spectroscopy.

References

[1] K. J. Friston, A. P. Holmes, K. J. Worsley, J. B. Poline, C. D. Frith, and R. S. J. Frackowiak, "Statistical parametric maps in functional imaging: A general linear approach," *Hum. Brain. Mapp.*, vol. 2, no. 4, pp. 189–210, 1995.

[2] Y. Oku, H. Masumiya, and Y. Okada, "Postnatal developmental changes in activation profiles of the respiratory neuronal network in the rat ventral medulla," *J. Physiol.*, vol. 585, no. 1, pp. 175–186, 2007.